

Impacts of Mountain Topography and Background Flow Conditions on the Predictability of Thermally Induced Thunderstorms and the Associated Error Growth

PIN-YING WU^{a,b,c} AND TETSUYA TAKEMI^a

^a *Disaster Prevention Research Institute, Kyoto University, Kyoto, Japan*

^b *Japan Meteorological Business Support Center, Tokyo, Japan*

^c *Meteorological Research Institute, Japan Meteorological Agency, Tsukuba, Japan*

(Manuscript received 17 December 2021, in final form 28 December 2022)

ABSTRACT: Thermally induced thunderstorm simulations were conducted with the Weather Research and Forecasting (WRF) Model in an idealized configuration to investigate the associated error growth and predictability. We conducted identical twin experiments with different topography and background winds to assess the impacts of these factors. The results showed that mountain topography restrains error growth at the early stage of convection development. This topographic effect is sensitive to mountain geometry and background winds: it was more noticeable in cases with higher and narrower mountains and difficult to see without background wind. The topographic effect and its sensitivity resulted from the different natures of convection initiation. However, the topographic effect became less apparent when moist convection continued growing and triggered rapid error growth. The predictability of thunderstorms is then limited at the timing after the convective activity reached its maximum. A smaller initial error or starting a simulation at a later time did not break this timing of predictability limit. Mountain topography also limitedly affected the timing of the maximum convective activity and the predictability limit. In contrast, background flows changed the convection evolution and the following predictability. The predictability limit assessed by rainfall suggested other aspects of the topographic effect. The domain-scale rainfall distribution and the intense accumulated rainfall can be adequately captured in the presence of mountains.

KEYWORDS: Convective clouds; Topographic effects; Numerical weather prediction/forecasting

1. Introduction

The atmosphere is a chaotic system with limited predictability. In numerical weather prediction (NWP), due to the error growth nature of a chaotic system, the predictable time range cannot be extended infinitely, even by minimizing model initial errors toward an infinitesimally small value (but not exactly equal to zero) (Palmer et al. 2014). Since Lorenz (1969) proposed a scale-dependent predictability concept of multiscale flows, atmospheric predictability has been widely investigated at different scales of atmospheric motion with various numerical models, from relatively idealized models of turbulent flows (Rotunno and Snyder 2008; Durran and Gingrich 2014; Sun and Zhang 2020) to complicated global (Ngan and Eperon 2012; Froude et al. 2013; Judt 2020) or regional (Leoncini et al. 2010; Weyn and Durran 2018; Potvin et al. 2017) numerical weather prediction models.

In the past two decades, benefiting from the improvement in computing power and NWP model, studies have extensively investigated error growth and predictability using convection-permitting models that allow moist convection to be explicitly represented (e.g., Melhauser and Zhang 2012; Nielsen and Schumacher 2016; Weyn and Durran 2017; Sun et al. 2017; Judt 2020; Zhuang et al. 2020). Many of these studies have indicated that moist convection is crucial for characterizing rapid error growth. Zhang et al. (2003) conducted numerical experiments for a snowstorm and showed that errors grow slowly when the latent heat of condensation is artificially set to zero.

Subsequently, Hohenegger et al. (2006), Selz and Craig (2015), and Zhang et al. (2016) showed that rapid initial error growth is associated with moist convection development or precipitation. The rapid error growth associated with moist convection limits atmospheric predictability (Sun and Zhang 2016; Judt 2018; Zhang et al. 2019).

Besides the error growth associated with moist convection that limits predictability at synoptic scales, error growth and predictability at meso- and convective scales have been receiving increasing attention. Several studies have investigated the error growth dynamics in simulations of various phenomena at meso- and convective scales (Hohenegger and Schär 2007a,b; Leoncini et al. 2010; Durran and Weyn 2016; Miglietta et al. 2016; Zhuang et al. 2020). Zhang et al. (2007) explored meso-scale error growth dynamics in idealized moist baroclinic waves. They indicated that errors growing from a small scale saturate at convective scales in approximately one hour and subsequently grow to larger scales, limiting the predictability of weather at synoptic scales. On the other hand, Durran and Weyn (2016) and Weyn and Durran (2017) evaluated the growth of initial errors introduced at different spatial scales using simulations of convective systems. They emphasized the need to reduce errors at a larger scale.

While different error growth dynamics have been proposed, most previous studies showed a convective-scale predictability limit of several hours (Hohenegger and Schär 2007a; Selz and Craig 2015; Weyn and Durran 2017; N. Wu et al. 2020). However, the predictability at meso- and convective scales is highly flow dependent and varies from case to case (Walser et al. 2004; Done et al. 2012; Johnson et al. 2014). The underlying dynamics, such as background flows (Zhang and Tao

Corresponding author: Pin-Ying Wu, pyingwu12@gmail.com

DOI: 10.1175/JAS-D-21-0331.1

© 2023 American Meteorological Society. For information regarding reuse of this content and general copyright information, consult the AMS Copyright Policy (www.ametsoc.org/PUBSReuseLicenses).

2013; Weyn and Durran 2017) or synoptic-scale weather conditions (Weyn and Durran 2019; Zhuang et al. 2020), affect convection development and the associated error growth properties and predictability. It is difficult to reach a universal predictability estimation applicable to various weather phenomena at convective scales. While increasing attention has been being paid, further investigations are still needed to explore convective-scale predictability for different weather phenomena and assess factors that may affect predictability at convective scales.

In the previous studies that investigated the predictability of convective-scale phenomena, minimal attention has been given to thermally induced thunderstorms in solar radiation diurnal cycles. A thermally induced thunderstorm is a universal phenomenon in the warm seasons under weakly forced synoptic-scale conditions (e.g., Wallace 1975; Kerns et al. 2010; Nomura and Takemi 2011); it is characterized by a short-lived time of one to a few hours and horizontally localized spatial extent at $O(10)$ km. Thunderstorms can bring sudden localized rainfall or strong winds on fair weather days, influencing people's daily lives and sometimes inducing property and human life losses (Changnon 2001). Predicting thunderstorms using NWP models could suffer from insufficient resolution (Schmidli et al. 2018) or incorrect initial conditions (Cheng et al. 2020) and is challenging in operational weather centers nowadays. However, through continuous improvement of computing power and the ongoing development of NWP models (Bauer et al. 2015), better simulation of weathers at convective scales are expected. With improved NWP models, future predictions of thunderstorms should also advance. Despite, the intrinsically limited predictable range for thunderstorms, which cannot be overcome even with nearly perfect models and initial conditions, is considered short because of their small characteristic scale and the rapid error growth associated with moist convection. The predictability limits must be understood to develop and utilize NWP efficiently and achieve optimum performance in predicting localized phenomena, such as thunderstorms. Thus, further investigation is desirable.

Besides exploring the limits of predicting thunderstorms, different factors affecting convection development and predictability must be examined to advance our understanding. For example, topography is a factor affecting the development of moist convection and probably the associated predictability (Carbone et al. 2002). Topography could induce different heating and cooling between elevated mountains and the surrounding valley or plain, driving diurnally varying circulation (Vergeiner and Dreiseitl 1987; Whiteman 1990; Demko et al. 2009) and affecting the generation and development of thermally induced thunderstorms in a diurnal cycle. During warm seasons, clear rainfall diurnal cycles are usually observed around mountain areas (Kerns et al. 2010; Nomura and Takemi 2011; Takemi 2014). However, in previous studies on predictability, the impact of topography has not been sufficiently addressed.

Recently, Bachmann et al. (2019, 2020) investigated the impact of topography on the predictability of moist convection from a practical perspective. They evaluated the forecast skills of rainfall with scores at different scales and showed that with

topography, reliable rainfall predictions are available at a finer scale. Wu and Takemi (2021, hereafter WT21) also showed the impact of mountain topography on decreasing the error growth associated with moist convection. Overall, topography is expected to impact error growth and rainfall predictability at a convective scale. However, the impact of topography on the predictability limit of thunderstorms remains unanswered. Also, the impact of the different sizes of mountains on error growth or predictability has been unexamined. The mountain's height or width impacts the development of moist convection and the accompanying rainfall amount and distribution (Flesch and Reuter 2012; Imamovic et al. 2019; Mulholland et al. 2020). A study should assess whether this sensitivity to mountain geometry is reflected in the error growth or predictability limit.

Furthermore, the presence of prevailing winds complicates influences of topography on the development of thunderstorms. Background flow conditions affect the organization of convective clouds (Takemi and Rotunno 2003; Fu and Guo 2012; Muller 2013) and the generation of thunderstorms over mountainous areas (Banta and Schaaf 1987; Carbone et al. 1995; Chen and Lin 1997). The impacts of topography and background flows are intertwined; mountain topography could change the distribution of flows to trigger convection, and the effects of background flow on convection could differ with different topography. Thus, it is desirable to examine the impact of topography and background flows on the predictability of thunderstorms simultaneously.

To address the above concerns, identical twin experiments were conducted using simulations of thermally induced thunderstorms in idealized configurations with different topography and background winds. The twin experiments were initialized before convection initiation (CI) to investigate the error growth dynamics associated with the entire development process of thunderstorms. By using identical twin experiments in a perfect model context, an upper limit for predicting thunderstorms was examined. Focusing on the impact of topography and background flows, the following issues were assessed:

- The topographic effects on error growth shown in WT21 and its sensitivity to mountain geometry and background winds
- The predictability limit of thermally induced thunderstorms and the accompanying rainfall estimated by the error growth of model state variables and the difference in rainfall field

The rest of this paper is organized as follows: Section 2 provides the model configuration, experimental settings, and the metrics used to assess predictability, together with a brief introduction to the simulation results. The sensitivity of error growth to mountain geometry and background flow conditions is assessed in section 3. Section 4 investigates the predictability limit of thermally induced thunderstorms and the accompanying rainfall. Section 5 discusses the cause of the topographic effect on error growth and its sensitivity in more detail. The summary is presented in section 6.

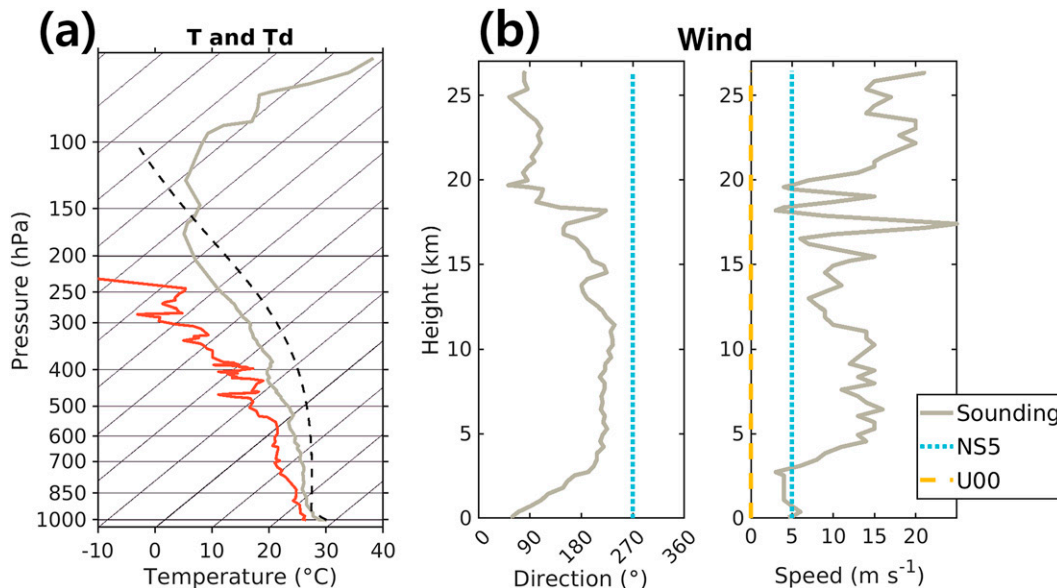


FIG. 1. (a) The profiles of temperature (gray) and dewpoint temperature (red) from the sounding data. (b) The profile of (left) wind direction and (right) wind speed from the sounding data (gray) and the ideal ones used in NS5 (dotted blue) and U00 (dashed yellow) experiments. The dashed black curve in (a) shows a reference for the adiabatic lapse rate of a parcel rising from the surface with the same temperature and moisture fields as the sounding data.

2. Numerical simulations and metrics for assessing predictability

a. Model configuration and experimental settings

The model configurations in this study followed those used in WT21. The Weather Research and Forecasting (WRF) Model version 4.2.1 is utilized with the same dynamics options and physics parameterizations as in WT21. The computational domain covers a horizontal area of $300 \text{ km} \times 300 \text{ km}$ resolved at 1-km grid spacing (i.e., 300×300 horizontal grid points). The model top is 25 km, and the number of vertical levels is 50. At the lateral boundaries, a doubly periodic condition is imposed. The thunderstorm simulations were initialized from the sounding data used in WT21 (Fig. 1; also refer to Fig. 1 in WT21). The temperature and moisture profiles from the sounding data provide a favorable condition for the development of deep convection with almost zero convective inhibition (CIN), and the height of the lifted condensation level is almost the same as the level of free convection (LFC), which is around 1-km height.

The design of identical twin experiments follows that of WT21. The horizontally homogeneous conditions derived from the sounding data were used to start a control simulation at 0000 local time (LT) 22 June. After the control simulation is spun up for 30 h, a perturbed simulation is initialized at 0600 LT before the initiation of moist convection. The perturbed simulation is initialized by randomly adding uncorrelated small differences to the water vapor mixing ratio of the control simulation at each model grid point. These small differences belong to a Gaussian distribution with zero mean and variance equal to 0.01 g kg^{-1} . Additional sensitivity tests with the perturbation only added to low levels below 2 km

showed similar error growth dynamics in the experiment with and without topography (figure not shown). The initial perturbation on water vapor is commonly used to investigate the predictability associated with moist convection (e.g., Weyn and Durran 2017, 2019). Also, the initial condition of the moisture field is crucial for predicting heavy rainfall (e.g., P.-Y. Wu et al. 2020). Since the phenomena of interest here are moist convection and the accompanying rainfall, we added perturbation to water vapor to evaluate the error growth caused by initial uncertainty in the moisture field. There were experiments with initial error on potential temperature, and the results show similar relative performance among experiments with different topography and background winds.

To assess predictability limit, we also performed the perturbed simulations with the initial perturbation of 0.1 and 10 times 0.01 g kg^{-1} , and the perturbed simulations started at later times of 0800 and 1000 LT with the original (0.01 g kg^{-1}) initial error magnitude. For convenience, the term “experiment” will be used for a simulation group that contains a control simulation and its perturbed simulation(s). For each experiment, the control simulation was initialized with a prescribed topography and a specific wind profile, and the perturbed simulation(s) were initialized by adding perturbations to the control simulation. The errors of each perturbed simulation were assessed using their differences from the corresponding control simulation.

Several experiments were conducted to investigate the impact of mountain geometry and background flows (Table 1). First, the original wind profile of the sounding data (ORI) was used, and different topography settings were performed. The first two experiments are without and with mountain

TABLE 1. Experiment names and their topography settings, and the initial wind profiles.

Wind profile for initial conditions	Expt	Mountain height (m)	Mountain volume	Mountain location (km)
Original sounding (ORI)	ORI_H00W00 (same as FLAT in WT21)	—	—	—
	ORI_H10W50 (same as TOPO in WT21)	1000	—	$x = 75, y = 100$
	ORI_H10W35	500	Halved	$x = 75, y = 100$
	ORI_H10W70		Doubled	$x = 75, y = 100$
	ORI_H05W70		—	$x = 75, y = 100$
	ORI_H05W50		Halved	$x = 75, y = 100$
	ORI_H05W100		Doubled	$x = 75, y = 100$
Zero wind (U00)	U00_H00W00	—	—	—
	U00_H10W50	1000	—	$x = 50, y = 150$
	U00_H10W35		Halved	$x = 50, y = 150$
	U00_H10W70		Doubled	$x = 50, y = 150$
Constant wind = 5 m s^{-1} (NS5)	NS5_H00W00	—	—	—
	NS5_H10W50	1000	—	$x = 50, y = 150$
	NS5_H10W35		Halved	$x = 50, y = 150$
	NS5_H10W70		Doubled	$x = 50, y = 150$

topography corresponding to the experiment FLAT and TOPO in WT21, respectively. In this study, we will refer to FLAT and TOPO as ORI_H00W00 and ORI_H10W50, respectively, to maintain a consistent naming scheme for all the experiments with different topography and background winds. The mountain in ORI_H10W50 is a 1000-m-height Gaussian-shaped mountain with around 50-km width embedded to the southwest of the domain (centered at $x = 75 \text{ km}$, $y = 100 \text{ km}$; see Fig. 2e). The location of the mountain was determined following the northeast movement of convective clouds to keep the clouds developing near the mountain remaining in the domain as long as possible. This made the analysis more intuitive. The choice of mountain height was based on the overall elevation of the Kii Peninsula, Japan, where the sounding data are located; in the Kii area, there is a pronounced diurnal cycle of thunderstorm-associated precipitation in the summer (Takemi and Tsuchida 2014). To examine the impact of mountain geometry, we changed the height or volume of the mountain here, inspired by Imamovic et al. (2019), who showed the mountain volume's impact on moist convection and accompanying rainfall amount. For example, the experiment having the mountain with the same height but halved and doubled volume (i.e., $\sqrt{0.5}$ and $\sqrt{2}$ times the width) of the mountain compared to ORI_H10W50 were referred to as ORI_H10W35 and ORI_H10W70, respectively. Additionally, ORI_H05W70 was the experiment in which the mountain height was reduced by half while maintaining the same volume (i.e., the width is $\sqrt{2}$ times) as in ORI_H10W50.

To investigate the impact of background flow conditions, besides the ORI experiments, the wind profile used to initialize the control simulation was replaced with either zero (U00) or westerly 5 m s^{-1} uniformly in the vertical direction (NS5), representing the conditions of no background wind and no vertical wind shear, respectively (Fig. 1b). The initial wind field in the control simulations was equal to zero in the U00

experiments and to 5 m s^{-1} in the NS5 experiments at all three-dimensional model grid points. These experiments with different background winds were also performed with and without mountain topography (Table 1). The wind field in the NS5 experiments was maintained westerly during the computation period, making the convective clouds move toward the east. Therefore, the mountain here is located within the western part of the domain (centered at $x = 50 \text{ km}$, $y = 150 \text{ km}$; see Fig. 2h), differing from the ORI experiments. The mountain location in the U00 experiment follows the NS5 one.

b. Metrics for assessing error growth and predictability

The predictability limit of thermally induced thunderstorms and the accompanying rainfall is evaluated by comparing the differences in model state variables and the simulated rainfall, respectively, between the control and perturbed simulations in each twin experiment. A proposed metric called convective moist difference total energy (CMDTE) was used to estimate the differences in model states. The fractions skill score (FSS; Roberts and Lean 2008) was applied to assess the difference in rainfall field. Detailed descriptions of the two metrics are provided subsequently.

The CMDTE used here follows the metric in WT21 but includes the differences in vertical velocity to consider the distinction of the convective cores. It is calculated at three-dimensional model grid points using the differences in the three-dimensional wind (u' , v' , w'), temperature (T'), water vapor mixing ratio (q_v), and surface pressure (p'_s) as follows:

$$\text{CMDTE} = \frac{1}{2} \left[u'^2 + v'^2 + w'^2 + \frac{c_p}{T_r} T'^2 + \frac{L_v^2}{c_p T_r} q_v'^2 + RT_r \left(\frac{p'_s}{p_r} \right)^2 \right]. \quad (1)$$

Here, T_r and p_r are the reference temperature (270 K) and reference pressure (1000 hPa), respectively, following the

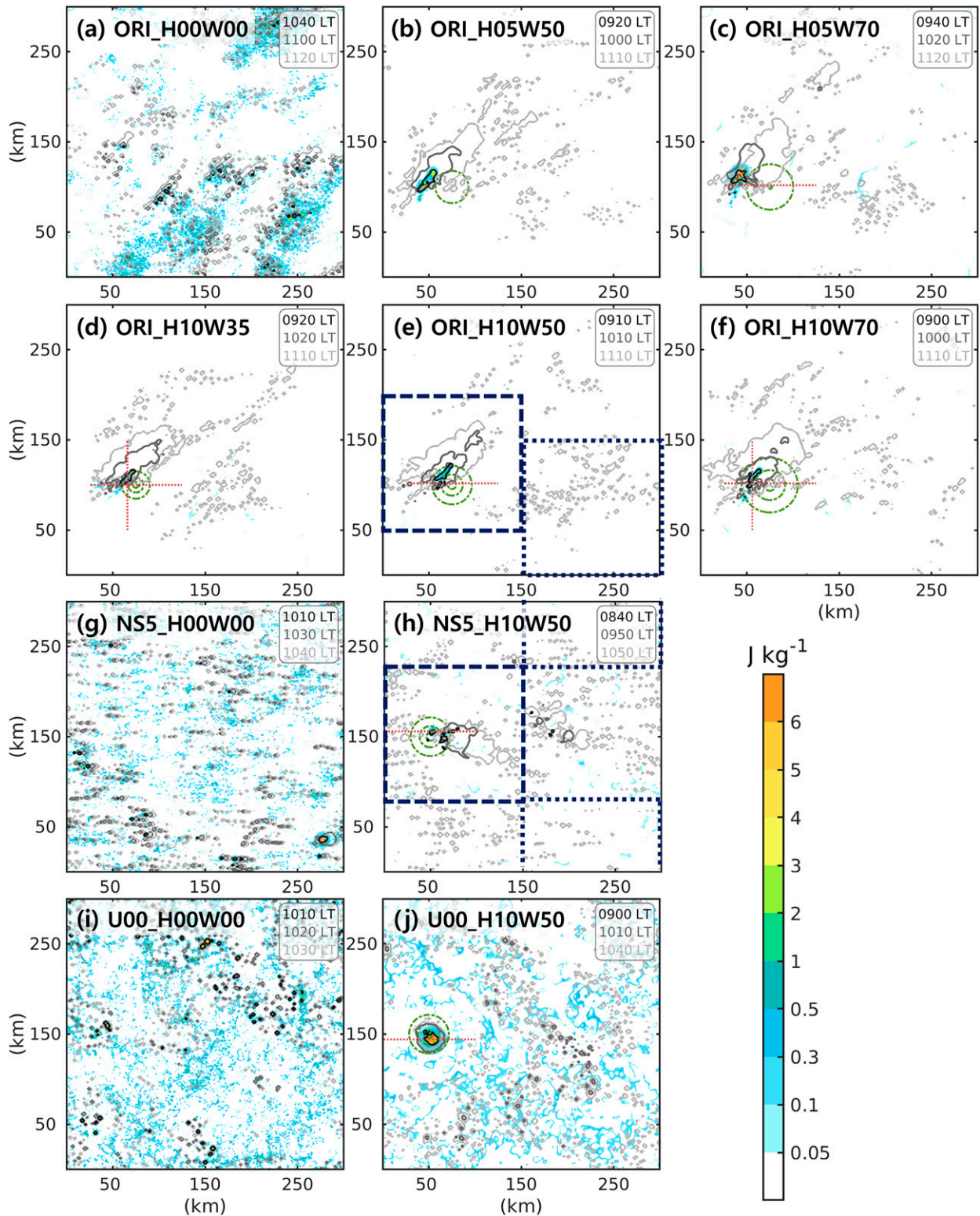


FIG. 2. The CMDTE at the time when the cloudy-point ratio is equal to 0.1% (color shaded) in (a) ORI_H00W00, (b) ORI_H05W70, (c) ORI_H05W50, (d) ORI_H10W35, (e) ORI_H10W50, (f) ORI_H10W70, (g) NS5_H00W00, (h) NS5_H10W50, (i) U00_H00W00, and (j) U00_H10W50. The contours depict vertically integrated hydrometeors equal to 0.7 kg m^{-2} (i.e., the definition of the cloud grid point) when the cloudy-point ratio is equal to 0.1%, 1%, and 5% (black, gray, and light gray contours, respectively). The times of the contours are depicted by the numbers with the same color in the upper right of each panel. The green dashed-dotted contours depict terrain heights of 100, 500, and 900 m. The red dotted lines show the location of the cross section depicted in Figs. 11–13. The dark-blue dashed boxes depict the subdomains for producing Figs. 5 and 14 and the mountain areas in Fig. 7; the dark-blue dotted boxes depict the subdomains for the plain areas in Fig. 7.

values used for the moist total energy norm in [Ehrendorfer et al. \(1999\)](#); c_p , L_v , and R are the specific heat capacity at constant pressure ($1004.9 \text{ J kg}^{-1} \text{ K}^{-1}$), the latent heat of condensation ($2.4359 \times 10^6 \text{ J kg}^{-1}$), and the specific gas constant of dry air ($287.04 \text{ J kg}^{-1} \text{ K}^{-1}$), respectively. Compared with the metrics used in previous studies, such as the difference total energy ([Zhang et al. 2003](#)), CMDTE involves the differences in vertical wind and water vapor, which are important components for developing moist convection, to better represent the error growth associated with predicting thunderstorms. The CMDTE presented in the following sections was calculated at each model grid point in the context that small displacements of convection were considered errors.

To assess the difference in rainfall field, we computed FSS using the rainfall of the control simulation as “observation” O_r , and the rainfall of the perturbed simulation as “model forecast” M_r . The rainfall fields O_r and M_r were first converted into binary fields I_o and I_M by setting the value to 1 at grid points for rainfall amounts above a predefined threshold and 0 at other points. These binary fields I_o and I_M are then used to generate the fractions $O(n)(i, j)$ and $M(n)(i, j)$ with the following equations:

$$O(n)(i, j) = \frac{1}{n^2} \sum_{k=0}^{n-1} \sum_{l=0}^{n-1} I_o(i+k, j+l), \quad (2a)$$

$$M(n)(i, j) = \frac{1}{n^2} \sum_{k=0}^{n-1} \sum_{l=0}^{n-1} I_M(i+k, j+l), \quad (2b)$$

where i and j are the indices of the computation domain in the x and y directions, respectively; n determines the square kernel range, whose size is $n \times n$, for generating the fractions. Since the doubly periodic condition is used, the neighborhood points over the lateral boundary of the computation domain are accounted for cyclically. The above equations make the square kernel centered at the point $[i + (n-1)/2, j + (n-1)/2]$, but not (i, j) , which is different from the ones in [Roberts and Lean \(2008\)](#). Since only the domain-averaged FSS was compared, the different formulas did not affect the results. The FSS is calculated as follows:

$$1 - \frac{\text{MSE}_{(n)}}{\text{MSE}_{(n)\text{ref}}},$$

where

$$\text{MSE}_{(n)} = \frac{1}{N_x N_y} \sum_{i=1}^{N_x} \sum_{j=1}^{N_y} [O_{(n)ij} - M_{(n)ij}]^2,$$

$$\text{MSE}_{(n)\text{ref}} = \frac{1}{N_x N_y} \left[\sum_{i=1}^{N_x} \sum_{j=1}^{N_y} O_{(n)ij}^2 + \sum_{i=1}^{N_x} \sum_{j=1}^{N_y} M_{(n)ij}^2 \right].$$

Here, N_x and N_y are the grid point numbers of the computation domain in the x and y direction, respectively. A higher FSS means a better agreement between O_r and M_r , and the best value of FSS is 1. Changing the size of kernel n allows the calculation of the FSS to consider neighboring rainfall in

different ranges, providing the estimate of rainfall accuracy at various scales. FSS is widely used to verify the NWP model’s rainfall prediction and to estimate the predictability of convective-scale events ([Weyn and Durran 2019](#)). Following previous studies (e.g., [Roberts and Lean 2008](#); [Weyn and Durran 2019](#)), we defined the FSS skillful criterion by $0.5 + f_0/2$, where f_0 is the ratio of points exceeding the predefined rainfall threshold in the computation domain. A rainfall prediction with an FSS higher than the skillful criterion is considered useful.

Comparisons using the two metrics, CMDTE and FSS, complement each other. [Weyn and Durran \(2019\)](#) showed that the metrics used to estimate the errors of NWP could change the interpretation of forecast skill and predictability. In this study, CMDTE is a metric that estimates the difference in the atmospheric states simulated at each model grid point; similar measurements are commonly used in predictability studies (e.g., [Lorenz 1969](#); [Zhang et al. 2003](#); [Weyn and Durran 2017](#)). On the other hand, FSS, which estimates the rainfall resulting from the simulated thunderstorms, provides a more practical view for assessing the predictability of thunderstorms since rainfall prediction is more often used in daily weather forecasts or disaster prevention. FSS is also used to assess the impact of topography and background winds at different spatial scales to complement the analysis of CMDTE at the model grid spacing scale.

c. Overview of the simulation results and the detection of cloud areas

[Figures 2 and 3](#) show an overview of convection development and rainfall in experiments with different topography and background winds. All the experiments reproduced the simulation of thermally induced thunderstorms similar to those in [WT21](#), while the start time and the patterns of convective clouds differed among the experiments ([Fig. 2](#)). During the entire computation period, the wind field in all experiments generally keep the condition given by the initial wind profiles, except for the area blocked by the mountain or where convective clouds were developing. Therefore, in experiments with different background winds, convective clouds have different orientations and movements corresponding to the wind conditions provided by the initial wind profile. Despite, as shown in [WT21](#), the experiments with mountain topography have terrain-induced convective clouds developing around the mountain at earlier times, regardless of the background wind; on the other hand, over the areas away from the mountain, convection develops similarly to those in nonmountain experiments at later times.

The rainfall distribution also shows the impacts of background winds and mountains ([Fig. 3](#)). The general orientation and size of the rain cells are different in the experiment with different background winds. Meanwhile, regardless of background wind, heavier and larger rainfall cells were observed over the mountain areas; in comparison, the rainfall distribution outside the mountain area was similar to that in the corresponding nonmountain experiment.

According to [WT21](#), error growth was influenced by convection development. Over areas where convective clouds

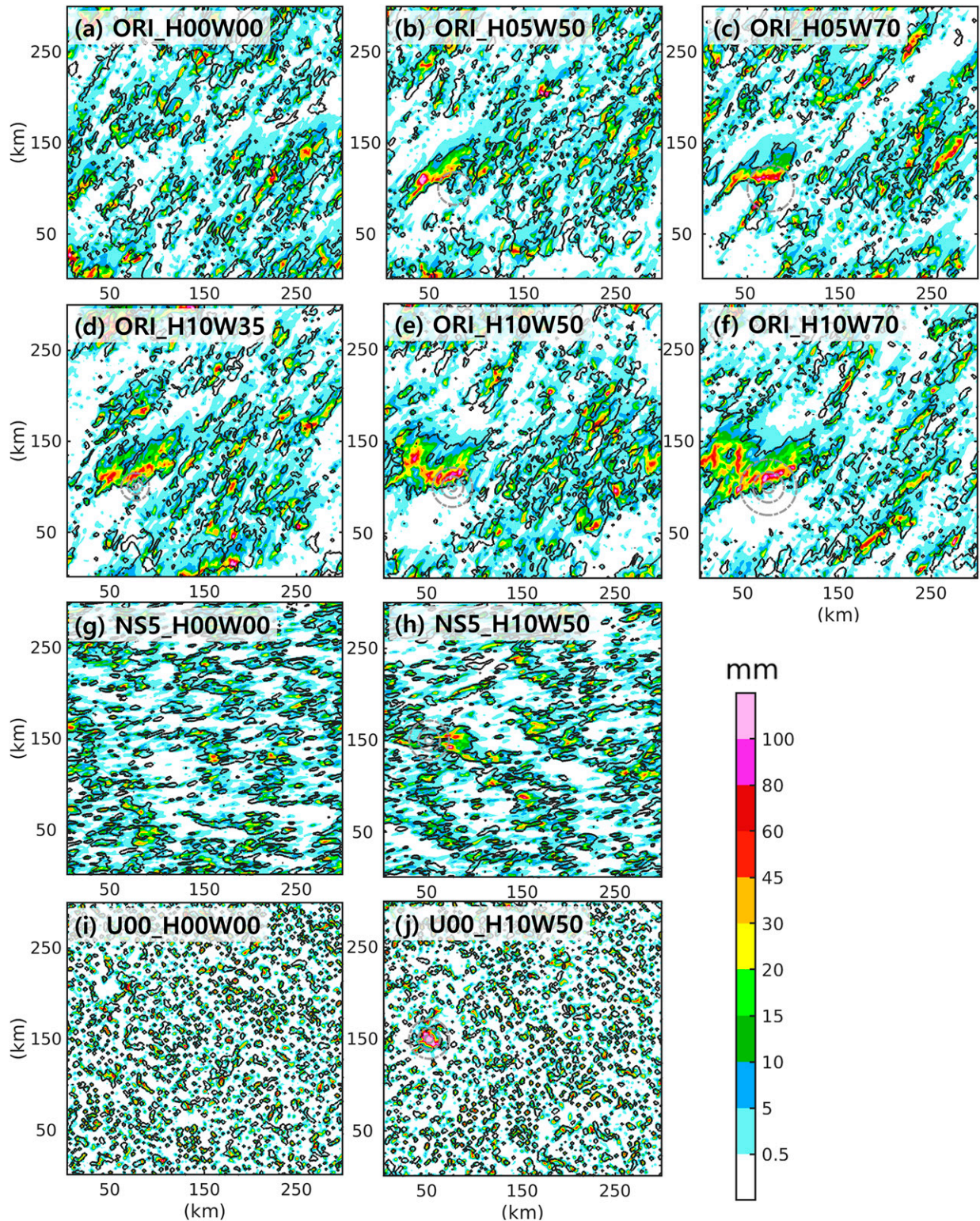


FIG. 3. The 12-h accumulated rainfall (from 0700 LT) of the control (color shaded) and perturbed (black contours, 5 mm) simulations in (a) ORI_H00W00, (b) ORI_H05W70, (c) ORI_H05W50, (d) ORI_H10W35, (e) ORI_H10W50, (f) ORI_H10W70, (g) NS5_H00W00, (h) NS5_H10W50, (i) U00_H00W00, and (j) U00_H10W50. The gray dashed-dotted contours depict terrain heights of 100, 500, and 900 m.

developed, errors grew quickly and were larger than those over areas without clouds (Fig. 3 in WT21). Figure 2 also shows similar CMDTE and convective cloud distributions in all the experiments. Consequently, the experiments having earlier convection development also have rapid error growth starting earlier. Thus, to compare the error growth among identical twin experiments having distinct features of convection development, the error growth was investigated in terms of the timing of moist convection development.

The reference for the timing of moist convection development was provided by identifying cloudy grid points representing where convective clouds were simulated in the model. Since the start times of convection are similar between the control and perturbed simulations in each twin experiment (Fig. 2 in WT21), the cloud grid point is identified using the control simulation. When a grid point has vertically integrated hydrometeor contents (i.e., the total of rainwater, cloud water, snow, graupel, and ice) larger than 0.7 kg m^{-2} , it is identified as a cloud grid point. The threshold of the vertically integrated hydrometeor contents corresponds to a simulated reflectivity of around 30 dBZ. Our additional analysis showed that changing the threshold to 0.3 or 1.5 kg m^{-2} does not affect the conclusion of this study (figure not shown). The purpose of the identified cloud grid point is not to define the exact stages of convection development but to provide a reference for comparing errors among different experiments with different convection development timings. We also define the cloudy-point ratio, which is the ratio of the identified cloud grid points to the total number of grid points over a computation domain, to represent the degree of convective activity. In the following, comparison of error will be provided based on the use of the defined cloud grid point.

3. The topographic effects on error growth

WT21 indicated that mountain topography could decrease the error growth associated with moist convection in its early stage of development. In this section, we examined the sensitivity of this topographic effect to mountain geometry and background flows.

Following the analysis in WT21 (their Fig. 6), the errors within the areas of individual convective clouds were compared (Fig. 4). A convective cloud area was defined as the continuous area of the cloud grid point having 10 grid points or larger. In Fig. 4, the cloud size is represented by the number of grid points in the detected cloud areas; the error magnitude was represented by the mean of the top 10 maxima vertical mass-weighted averaged CMDTE over the detected cloud areas. For the experiments with topography, only the scatter points of convective clouds detected before 1040 LT are depicted in Figs. 4a and 4b, and only those before 1020 LT are depicted in Figs. 4c and 4d. In the experiments with topography, free convection developed similarly to that in the nonmountain experiments at later times, resulting in similar scatterplots (Fig. 6 in WT21). These scatterplots of the convective clouds at later times overlap when depicting them together in Fig. 4, so they are omitted to make the comparison among the experiments more evident. The results of the

nonmountain experiments were presented in full whenever a cloud area was detected from 0800 to 1200 LT in a 20-min interval.

Using Fig. 4, we compared the errors among convective clouds of a similar size to address the topographic effects on error growth. Previous studies and our results showed that error growth is greatly related to the distribution of convective clouds (WT21; Fig. 2). Since the simulations were conducted in an idealized framework with the doubly periodic lateral boundary condition, there was no other considerable source of error growth comparable to moist convection. Error growth is presumed to be mainly caused by convection development. The convection at a similar stage, which might result in a similar size of convective clouds, is expected to trigger a similar error magnitude if the mountain topography has no impact.

We compared the ORI experiments to investigate the impact of mountain geometry (Figs. 4a,b). Here, ORI_H00W00 is a reference for the relationship between errors and cloud sizes in the nonmountain ORI case. The topographic effect was then assessed by how the results of the experiments with topography depart from the area possessed by ORI_H00W00. Compared with Fig. 4b, Fig. 4a shows more scatter points from the experiment with topography located away from the area possessed by the ORI_H00W00 results. Namely, some convective clouds in the experiments with 1000-m mountains triggered less error growth than in ORI_H00W00, while those in the 500-m mountain experiments resulted in error magnitudes comparable to the ones in ORI_H00W00. Figures 4a and 4b suggest that irrespective of the mountain width, the impact of mountains with 1000-m height is more pronounced than that of mountains with 500-m height. Additionally, when looking at mountains with the same height, the mountain width, although not as clearly as the mountain height, also affects error growth. For example, Fig. 4a shows that some convective clouds with the size of around 5 km in ORI_H10W70 have slightly larger errors than those in ORI_H10W35 and ORI_H10W50. Similarly, the errors in ORI_H05W70 tended to be larger than those in ORI_H05W50 (Fig. 4b).

Furthermore, we investigated error growth in different vertical levels during the time of CI in some ORI experiments (Fig. 5). To focus on the impact of topography, we calculated the horizontal average over a subdomain around the mountain topography (Fig. 2e). The same subdomain was used for ORI_H00W00. The choice of the subdomain barely changes the result of ORI_H00W00 since the convection in ORI_H00W00 develops fairly over the computation domain. In Fig. 5, the hydrometeors represent the development of moist convection in the vertical direction over time; the CMDTE shows the corresponding error growth. The θ anomaly (the differences of the θ at each grid point from the horizontally averaged θ) and the upward wind are also depicted to show the thermodynamic and dynamic states.

Figure 5 shows the exponential error growth following the convection development in the vertical direction and the different error growth rates among the experiments. In ORI_H00W00, moist convection developed upward quickly from 1020 LT. The errors at different vertical levels grow rapidly

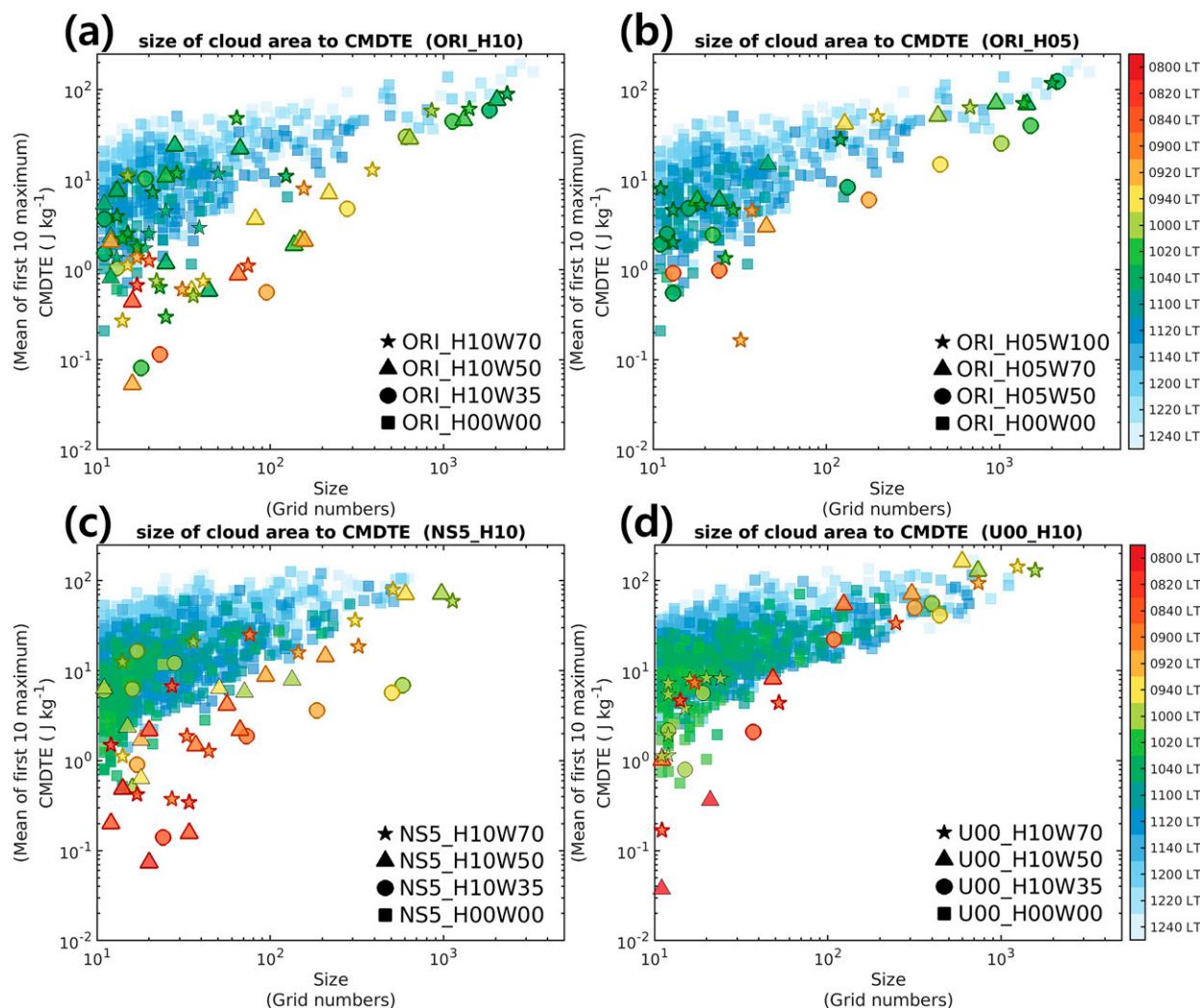


FIG. 4. Scatterplots of the convective cloud size (x axis) against CMDTE magnitude (y axis) in (a) the ORI experiments with 1000-m-height mountains, (b) the ORI experiments with 500-m-height mountains, (c) the NS5 experiments with 1000-m-height mountains, and (d) the U00 experiments with 1000-m-height mountains. The corresponding nonmountain (H00W00) experiment was added to each panel. Each scatter point represents the results from a detected cloud area in an experiment, depicted by different markers, at a time represented by the color. The scatter points with colored thicker edges represent the clouds detected near the mountains where the distance between the detected cloud center and the mountain top is shorter than 100 km.

by order of magnitude or greater immediately after the development of convective clouds to that level (Fig. 5a). In comparison, the error growth after convection starts developing is slower in ORI_H10W50, suggesting the topographic effect of a 1000-m mountain on restraining error growth over different vertical levels. For example, throughout the levels below 5 km, it takes more than 1 h for the error in ORI_H10W50 to grow from 10^{-3} to over $10^{-1} \text{ J kg}^{-1}$ after the convective cloud develops, while it only takes 20–30 min for the growth of error in ORI_H00W00.

The sensitivity of the topographic effect to the mountain geometry is also seen in Fig. 5. Here, the sensitivity to mountain height is presented by the comparison between ORI_H10W50 and ORI_H05W70, whose mountain widths are different, to demonstrate a more distinct difference. In ORI_H05W70, the exponential growth of error is much more rapid than in ORI_

H10W50 (cf. Figs. 5b,c). Throughout all the heights, the errors in ORI_H05W70 start exponential growth almost right after the development of convective clouds. This is similar to that of ORI_H00W00 (cf. Figs. 5a,c), suggesting less effect on restraining error growth. Similar sensitivity to mountain height is supported by comparing ORI_H10W50 and ORI_H05W50, as well as ORI_H10W70 and ORI_H05W70. The results of ORI_H05W50 (figure not shown) are very similar to those of ORI_H05W70, while the mountain width also played a role, and errors indeed grow slightly more rapidly in ORI_H05W70 than in ORI_H05W50. Also seen in Fig. 5 is the sensitivity to mountain width. In ORI_H10W35, while the vertical development of convective clouds seems similar to that in ORI_H10W50, the error grows more slowly than in ORI_H10W50 (cf. Figs. 5b,d). For example, at levels around 3–5 km, the error

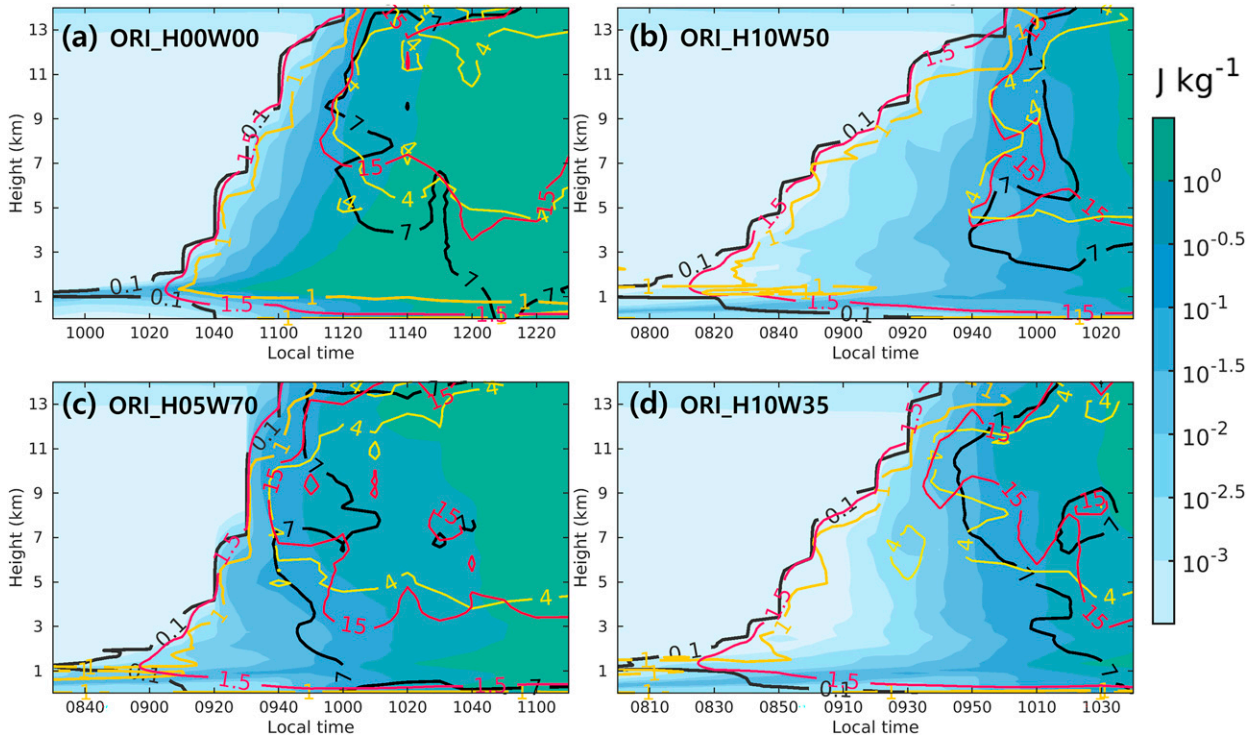


FIG. 5. The time–height cross section of the horizontally averaged CMDTE (color shaded), and the horizontally maximum of hydrometeors (black contours; 0.1 and 7 g kg^{-1}), upward wind (red contours; 1.5 and 15 m s^{-1}), and θ anomaly (yellow and bright yellow contours; 1 and 4 K, respectively) in the control simulation over a subdomain in (a) ORI_H00W00, (b) ORI_H10W50, (c) ORI_H05W70, and (d) ORI_H10W35. The dark-blue dashed box in Fig. 2e shows the range of the subdomain.

in ORI_H10W35 stays below $10^{-3} \text{ J kg}^{-1}$ for 20 min after the convection develops, while the error in ORI_H10W50 grows exponentially to $10^{-2.5} \text{ J kg}^{-1}$ in 20 min. Figures 5, 4a, and 4b suggest the same sensitivities of the topographic effect: the higher and narrower mountains have a clear impact on constraining error growth.

Besides the sensitivity to mountain geometry, the sensitivity of topographic effects to background winds is further examined (Figs. 4c,d). Here, we compare the experiments without topography and with 1000-m mountains to see if the same topographic effect also arises under different background winds. In the NS5 experiments, the results show a similar topographic effect to that in the ORI ones (cf. Figs. 4a,c). On the other hand, the topographic effect is less clear than in the ORI cases (cf. Figs. 4a,d); only a few points among the topography experiments show smaller errors than those of ORI_H00W00 when the cloud area sizes are below 10 km.

In this section, we showed the topographic effect, consistent with WT21, on both the error in individual clouds and the error over different vertical levels; we further demonstrated the sensitivity of this effect to mountain geometry and background winds. However, note that along with the development of convective clouds, the errors among the experiments became more similar in magnitude. The strong upward winds and enhanced latent heating promoted error growth in all experiments, even over the mountain area. In Fig. 5, for instance, when the upward wind and positive θ anomaly, indicating the intensity of moist convection,

reach 15 m s^{-1} and 4 K, respectively, the errors in all the experiments grow to a similar magnitude. Figure 4 also shows that even in the experiments showing the topographic effect, such as those in Figs. 4a and 4c, the convective cloud areas detected near the mountains at later times are likely to have error magnitudes comparable to those in the nonmountain experiments.

4. Predictability of thermally induced thunderstorms

The error growth natures in a chaotic system limit the predictability of the system. In other words, there exists an upper bound on the length of time for meaningful predictions. We have shown the topographic effect on error growth during the early stages of convection development and investigated the sensitivity of this effect. However, it is still not evident if there is a limit of predicting thermally induced thunderstorms and how topography and background winds impact the predictability. This section investigates the predictability limit of thermally induced thunderstorms and the impacts of topography and background winds. The CMDTE and FSS estimate the limit of predicting convective clouds and accompanying rainfall, respectively, from different aspects. The former offers a measure for the limit of predicting instantaneous states of thunderstorms at each grid point. The latter examines the limit of predicting rainfall, which is crucial information in weather forecasts, from a practical aspect and provides the assessment at various spatial scales.

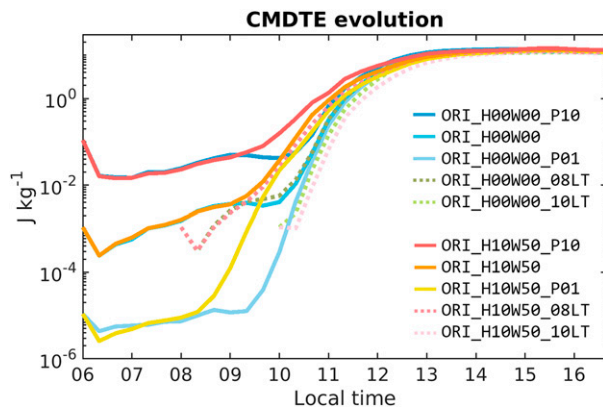


FIG. 6. Time evolution of the domain-averaged CMDTE between the control simulation and the perturbed simulations with initial error amplitudes equal to 0.1 g kg^{-1} (ORI_H00W00_P10 and ORI_H10W50_P10), 0.01 g kg^{-1} (ORI_H00W00 and ORI_H10W50; the original ones), and 0.001 g kg^{-1} (ORI_H00W00_P01 and ORI_H10W50_P01) started at 0600 LT and equal to 0.01 g kg^{-1} but started at 0800 LT (ORI_H00W00_08LT and ORI_H10W50_08LT) and 1000 LT (ORI_H00W00_10LT and ORI_H10W50_10LT).

a. Limit of predicting convective clouds

When the initial error growth reaches saturation, it is a sign of the limit to providing reliable prediction by NWP models and is usually used to imply a predictability limit (e.g., Judt 2018; Zhang et al. 2019). Here, we performed additional perturbed simulations with different initial error magnitudes and times to assess the predictability limit by the growth of the CMDTE. The control simulations in ORI_H00W00 and ORI_H10W50 are again used. Additional perturbed simulations are conducted by adding small differences in the water vapor mixing ratio with magnitudes of 0.1 and 0.001 g kg^{-1} (i.e., 10 and 0.1 times the original one, denoted as “_P10” and “_P01,” respectively) at 0600 LT and with the same magnitude (0.01 g kg^{-1}) but at 0800 and 1000 LT (denoted as “_08LT” and “_10LT,” respectively). These additional simulations are designed to examine whether using a smaller initial error or initializing the simulation later can extend the time of predictability limit implied by the error saturation (i.e., the time of losing the capacity to improve predictions).

Figure 6 shows the evolution of domain-averaged CMDTE between the control simulation and these additional perturbed simulations in ORI_H00W00 and ORI_H10W50. In both experiments, all the perturbed simulations indicated an error decrease just after the initial time, which is considered a spinup of random initial errors to get into a growth mode. After 0800 LT, errors start to grow exponentially. The rapid exponential error growth phase occurs earlier in the ORI_H00W00 set of simulations than in ORI_H00W00 due to the presence of terrain (see also WT21). Meanwhile, for the same simulation set of ORI_H00W00 or ORI_H10W50, the perturbed simulations started with smaller initial error magnitudes exhibit growth with larger orders of magnitudes during the exponential growth phase. This corresponds to Zhang

et al. (2003). Despite the different characteristics in the morning, error growth in all the perturbed simulations slows down after 1200 LT and reaches similar magnitudes at around 1300 LT, indicating an error saturation time. The similar error saturation time of the perturbed simulations with different initial error magnitudes implies the predictability limit of thermally induced thunderstorms. Meanwhile, the perturbed simulations initialized at different times also had a similar saturation time, resulting in an even shorter predictable range, highlighting the strong flow-dependent predictability at convective scales.

In Fig. 6, in addition, results of ORI_H00W00 and ORI_H10W50 show little difference in the timing of error saturation, indicating that the existence of topography affects little on the predictability limit. Subsequently, we examined the error saturation times of the experiments with different mountain geometry using the perturbed simulations initiated at 0600 LT with an error magnitude equal to 0.01 g kg^{-1} . Error evolutions (Fig. 7b) are depicted together with the cloudy-point ratio (Fig. 7a) and the ratio of errors to the cloudy-point numbers (Fig. 7c) to show the evolution of convective activity and the level of errors triggered by a unit number of convective clouds, respectively. Results over the mountain and plain subdomains are also presented separately to compare the error growth only near the mountain. Over both subdomains and the entire domain, error evolutions coincided with the evolution of the cloudy-point ratio for all the experiments. Over the plain area in the experiments with topography, the results are similar to that in the nonmountain experiment. Over the mountain area, Fig. 7c shows that the ratio of error to convective activity is smaller in the experiments with the 1000-m mountains over the mountain area around 0900 and 1000 LT. However, it becomes comparable to all other experiments and areas later. Namely, consistent with the results in section 3, over the mountain area, the same cloudy-point numbers triggered less error growth at early times. Nevertheless, the impact become little at a more developed stage of convective clouds. The fact of that the error growth over the mountain area is slower at first but becomes normal later highlights the strong flow-dependent predictability at convective scales, at which the error growth rate could increase quickly in response to the development of moist convection.

The little impact of the mountain on error growth at later times results in the convection development dominating error growth and the consequent limit of predictability. When assessing the entire domain-averaged CMDTE, all the ORI experiments showed a similar time of error saturation when convective activity reached the maximum (Figs. 7a,b). It is considered that the rapid error growth in response to more active moist convection near noon eventually results in error saturation at the time of maximum convective activity. Even starting the perturbed simulations later did not break this limit (Fig. 6). Similarly, in the experiments with topography, the maximum convective activity time decides the timing of losing predictability. Consequently, mountain topography, which also rarely affects the time of maximum convective activity over the entire domain, shows little impact on the predictability estimated by the domain-averaged error growth.

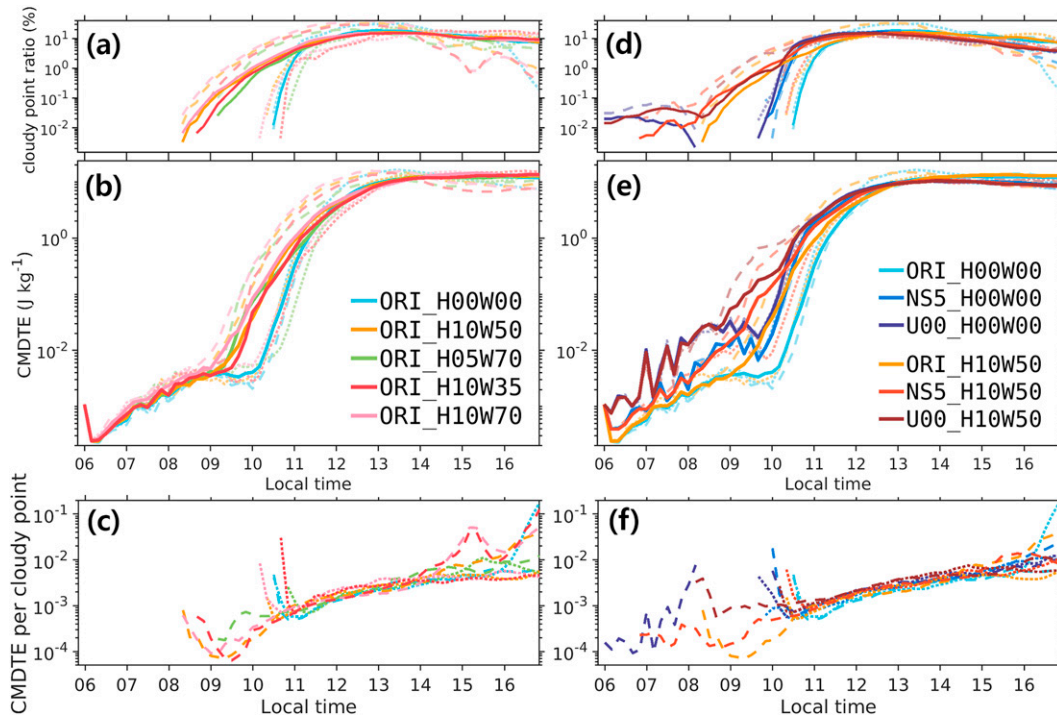


FIG. 7. Time evolution of (a),(d) the cloudy-point ratio, (b),(e) the CMDTE, and (c),(f) the ratio of CMDTE to cloudy-point numbers of experiments with different (a)–(c) topography and (d)–(f) background winds. See Table 1 for the settings of each experiment. The solid, dashed, and dotted curves represent the average taken over the entire domain, mountain area, and plain area, respectively. The mountain and plain subdomains, depicted in Fig. 2, are the same in the experiments with the same background wind. The entire domain-averaged results are omitted in (c) and (f).

Experiments with different background winds show evidence of the domination of convection development on flow-dependent predictability (Figs. 7d–f). When comparing the subdomain-averaged evolutions, the error growth generally coincides with the convective activity (Figs. 7d,e). The ratio of the error to convective activity (Fig. 7f) is also smaller over the mountain area in the mountain-included experiments of NS5 but not in U00_H10W50, consistent with the sensitivity suggested by Fig. 4. When comparing the entire domain-averaged evolution, it is not surprise that both the error and convective activity are affected by the background wind, considering the impact of flow conditions on convection development (e.g., Muller 2013; Fu and Guo 2012). For the NS5 and U00 experiments, the times of maximum convective activity were earlier than the ORI ones. The saturation time was consequently earlier in these experiments, regardless of whether the mountain existed. Consequently, Fig. 7 suggests that by affecting the convection development, the background winds have a greater impact on the time of predictability limit than the topography test in this study.

b. The predictability limit of rainfall brought by thunderstorms

Precipitation predictions are vital information in day-to-day weather forecasts. Although the error of model state variables, such as temperature and wind, are also important metrics for evaluating the ability of NWP, assessing the accuracy of rainfall prediction is even more critical from the practical viewpoint

of providing reliable NWP for daily weather forecasts. Here, we used the FSS (see section 2b) for estimating the difference in rainfall field between the control and perturbed simulations to assess the predictability of thunderstorm-accompanying precipitation.

The results of rainfall scores, different from the CMDTE shown previously, vary greatly in the afternoon when different initial random perturbations are added. Thus, for robustness, the results of additional perturbed simulations are included in this section. Four additional perturbed simulations were conducted against the control simulation by adding different random perturbations with an amplitude of 0.01 g kg^{-1} at 0600 LT (the same as the original one) using different random seeds. This provides five perturbed simulations with the same start time and amplitude of initial error in each identical twin experiment. The FSS was calculated separately between the control and the five perturbed simulations. The following presents rainfall scores using the mean of the five FSS calculated in each experiment. The skillful criteria of FSS are provided based on the rainfall fraction in the control simulation. When comparing the experiments with different background winds, we will depict the averaged criteria from the experiments having the same background wind since the experiments with the same background wind have similar rainfall evolution.

We first assess the FSSs with a rainfall threshold of 1 mm h^{-1} calculated at each model grid point, i.e., n in Eq. (2) is equal to 1 (solid curves in Fig. 8). In this context, a small shift of rainfall

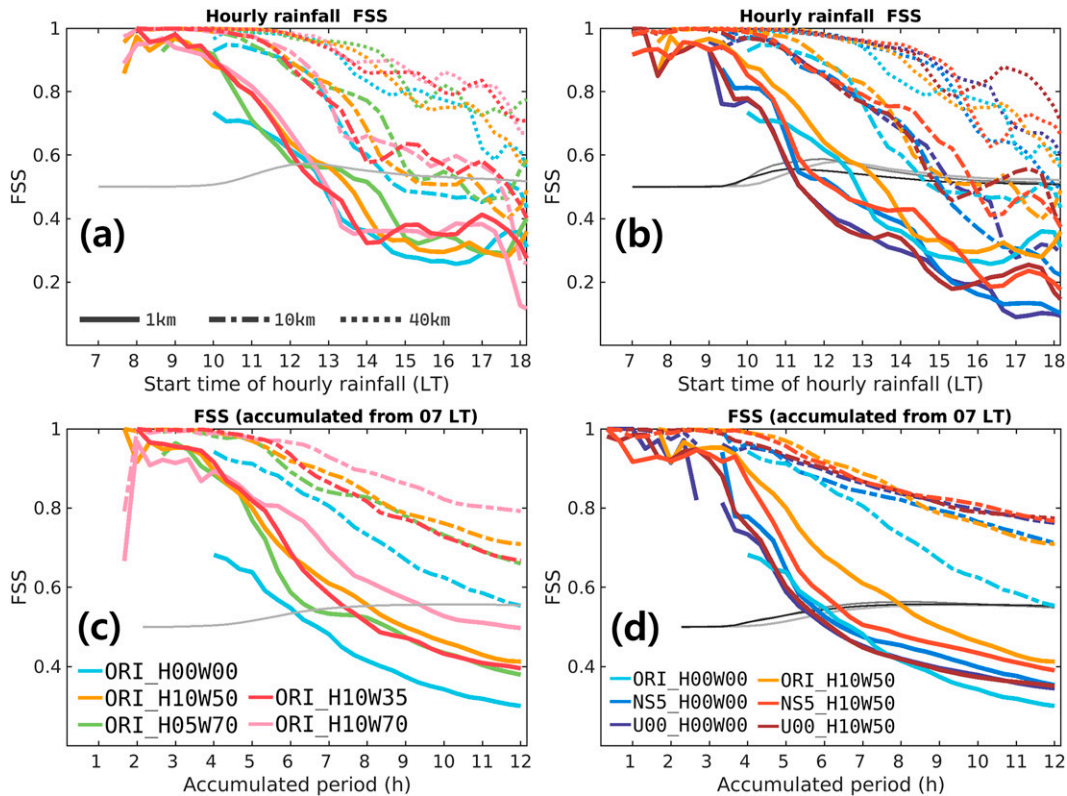


FIG. 8. FSS evolution of (a),(b) hourly rainfall and (c),(d) rainfall accumulated from 0700 LT. The FSSs with neighborhood sizes of 1, 10, and 40 grids are depicted in solid, dotted-dashed, and dotted curves. The scores were calculated in a 10-min interval from 0700 LT in all experiments. The x axis in (a) and (b) depicts the start time of hourly rainfall. The light gray, gray, and dark-gray curves show the skillful criteria in the ORI, NS5, and U00 experiments, respectively.

distribution is seen as the error caused by the growth of the initial perturbation; a strict estimate of predictability is provided. In the ORI experiments (Fig. 8a), the FSSs decreased rapidly after 1000 LT and become lower than the skillful criterion around 1200–1300 LT, regardless of the topography settings, suggesting that topography impacts little on the predictability of hourly rainfall at the model grid spacing scale. The experiments with different background winds (Fig. 8b) similarly showed a rapid decrease in FSSs after 1000 LT and little difference between the experiments with and without topography. However, experiments with different background winds have distinct performances. In NS5 and U00 experiments, the times of the FSSs becoming lower than the skillful criteria were earlier than those in the ORI experiments, suggesting a shorter predictable range in the NS5 and U00 experiments, which is also consistent with the result of the CMDTE. Overall, the hourly rainfall at the model grid spacing scale suggest similar conclusion as the CMDTE does; the predictability of thunderstorms and their accompanying rainfall was affected by background winds more greatly than the mountain topography tested in this study.

Conversely, the FSSs of several hours of accumulated rainfall at the model grid spacing scale show different sensitivities to the topographic effects (Figs. 8c,d). Here, the rainfall

threshold for computing FSSs is set to 1 mm h^{-1} . For 3-h accumulated rainfall, for example, the threshold for computing FSSs is 3 mm. The scores of accumulated rainfall estimate the predictability of the total rainfall brought by thunderstorms developing from the morning. An accumulated rainfall prediction is usually used as a metric for evaluating the potential for disasters like flooding to occur. Therefore, we assessed the impact of topography and background winds on this essential information in weather forecasts from a practical view point of disaster prevention. In the ORI experiments (Fig. 8c), ORI_H00W00 had lower accumulated rainfall FSSs throughout the 12-h accumulation period than other experiments with topography. Such topographic effects are also shown in the NS5 experiments (Fig. 8d). In NS5_H10W50, the FSSs are even higher than ORI_H00W00, which differs from hourly rainfall (cf. Figs. 8b,d). The higher FSSs in the experiments with topography, which is not seen in hourly rainfall, suggest that with the existence of mountain topography, the rainfall accumulated for several hours might be better predicted than in the case of flat topography, while the hourly rainfall might not. Additionally, the two U00 experiments showed fewer distinct FSSs of accumulated rainfall, highlighting that the impact of topography is intertwined with the background wind.

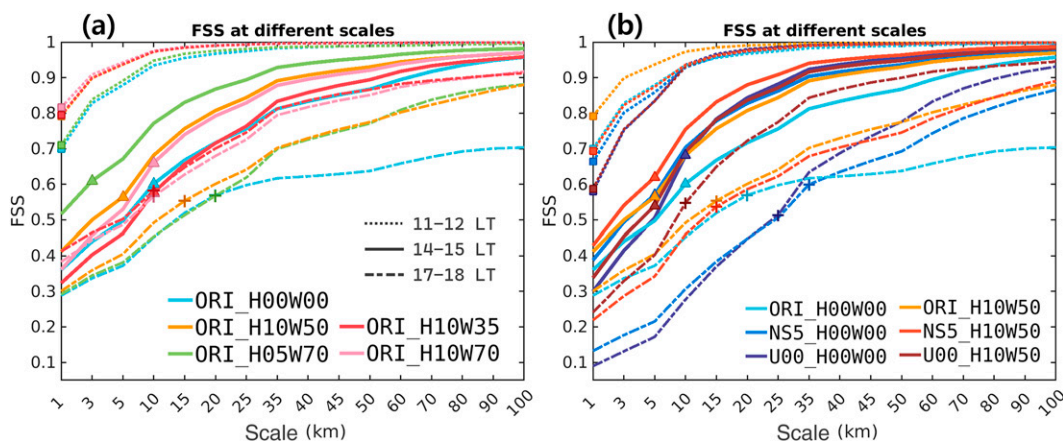


FIG. 9. The FSSs of hourly rainfall from 1100 (dotted), 1400 (solid), and 1700 LT (dashed–dotted). The x axis depicts the neighborhood sizes used to calculate the FSS. The square, triangle, and plus sign markers represent the measured useful scale at 1100, 1400, and 1700 LT, respectively.

Besides the scores at the model grid spacing scale, we also compared the FSS using different neighborhood sizes. Rainfall prediction with small spatial shifts is sometimes acceptable and could provide useful information in weather forecasts. For FSSs at the 10-km scale (dashed–dotted curves in Fig. 8), those of accumulated rainfall kept higher than the skillful criteria through the computation period in all the experiments; those of hourly rainfall also became lower than the skillful criteria at later times than the model-grid-scale FSSs, suggesting a longer predictable time at a larger scale. In the ORI experiments (Fig. 8a), all the experiments with mountain topography tended to have their FSSs higher than ORI_H00W00 at the 10-km scale. The FSSs of the experiments with topography generally continue keeping higher or comparable to the skillful criteria until 1700 LT. The experiments with different background winds also showed more distinct FSSs between the experiments with and without topography at 10 km than the model grid spacing scale. Meanwhile, the difference between the experiments with different background winds is also less clear compared to the FSSs at the model grid spacing scale.

In the U00 or NS5 experiments, the FSSs at larger scales were comparable to or higher than the ORI experiments when the experiments with the same topography setting were compared, different from those at the model grid spacing scale. The higher rainfall scores at larger scales in the NS5 and U00 experiments might result from the smaller characteristic spatial scale of convective cells and the rainfall pattern in these experiments (see Figs. 2 and 3). In this case, accounting for neighbor grids away from a grid point might include rainfall brought by different convective cells, making the estimate of large-scale rainfall distribution less punished. The higher scores of the NS5 and U00 experiments at larger scales could be interpreted as the rainfall at a larger scale is better predicted. However, it is difficult to certify the usefulness of this higher score at larger scales in the practical use of rainfall prediction when the characteristic spatial scale of rainfall is relatively small. The FSSs calculated on a larger scale (40 km)

suggest similar relative performance among the experiments as in the case of 10-km scale, while almost all experiments had higher FSSs than the skillful criteria until 1800 LT (dotted curves in Figs. 8a,b).

To further assess the rainfall predictability at different scales, Fig. 9 provides the FSSs at other scales and the assessment of a “useful scale,” which is the minimum scale on which the FSS becomes higher than the skillful criteria. Figure 9 corresponds with Fig. 8. The experiments with topography have higher FSSs at large scales than those without topography. The NS5 and U00 experiments also have higher scores at larger scales than the ORI experiment. The FSSs in the U00 experiments increase rapidly when the scale is larger than 5 km, especially in the afternoon. This inverse performance at scales smaller and larger than 5 km supports the previous assumption that a smaller typical spatial scale of convection results in less punishment of the FSSs at larger scales since the rainfall in the U00 experiments is distributed in cells with a 5–10-km range (Fig. 3). In ORI experiments (Fig. 9a), the assessed useful scale is larger in the nonmountain one than in others in the afternoon, implying that the experiments with topography have better prediction at a finer scale, which is consistent with Bachmann et al. (2019). At the scales over the useful scale, the distinction between the experiments with and without topography becomes even clearer at larger scales at 1700 LT, suggesting that topography plays a role in constraining the large-scale rainfall distribution.

The topographic effect at larger-scale rainfall distribution could come from the constraint of mountain topography on the overall generation and distribution of thunderstorms. While the exact location and structure of individual convective clouds are almost unpredictable in the afternoon, the convective clouds in the experiments with topography occur only outside the mountain area in the afternoon (Fig. 2 in WT21). The lack of CI around the mountain resulted from the evaporative cooling of rainfall in the morning, which generated relatively cool air at low levels. The cool air and the mountain as

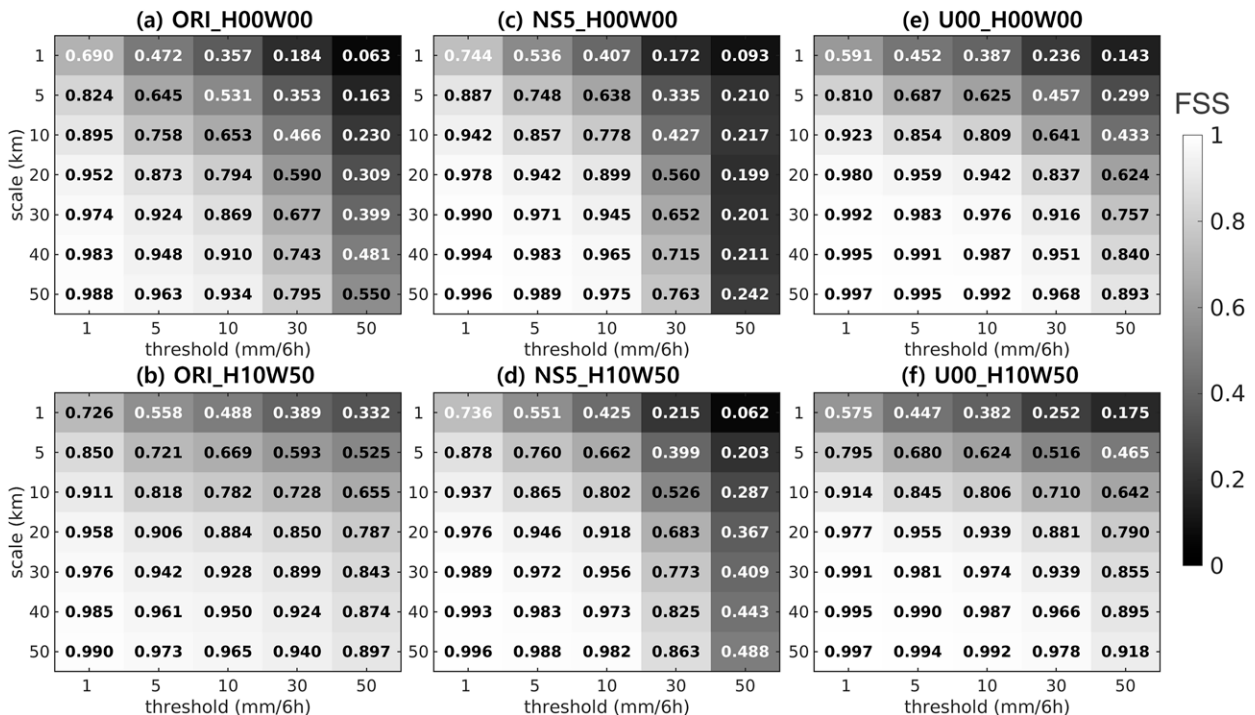


FIG. 10. The FSSs of the rainfall accumulated from 1000 to 1600 LT using different neighborhood sizes (y axis) and rainfall thresholds (x axis) in the experiment (a) ORI_H00W00, (b) ORI_H10W50, (c) NS5_H00W00, (d) NS5_H10W50, (e) U00_H00W00, and (f) U00_H10W50. The numbers in each grid depict the value of FSSs in black and white for those higher and low than the skillful criteria, respectively.

a block restrain CI and the movement of convective clouds near the mountain. Consequently, the domain-scale rainfall distribution was constrained. This constraint on domain-scale rainfall also explains the distinct performance of accumulated rainfall scores between experiments with and without topography. The accumulation of rainfall smoothed out small-scale structures, so the topographic effect on domain-scale rainfall distribution is highlighted in the distribution of accumulated rainfall.

Given the importance of accumulated rainfall predictions on practical utilization, such as disaster prevention and heavy rainfall warnings, we further calculated the FSSs of 6-h accumulated rainfall at different scales with varied predefined rainfall thresholds and assessed the impacts of topography. Figure 10 shows that experiments with topography have higher FSSs when the rainfall threshold is larger, regardless of the background winds. Higher scores for larger rainfall thresholds mean that the distribution of heavier rainfall is better captured. In the experiments with topography, convective clouds developed vigorously over the mountain area and brought heavier rainfall in the morning. This terrain-affected rainfall is distributed more similarly in the control and perturbed simulations than the rainfall over plain areas (Fig. 3), which could be the main cause of the higher FSSs for larger rainfall thresholds. Besides the topographic effect on large-scale rainfall distribution, Fig. 10 suggests that, with the existence of mountain topography, the heavy rainfall could be better predicted.

Overall, the assessment using the FSS of rainfall complements the estimation of the predictability limit provided by the CMDTE. Although topography minimally affects the predictability of hourly rainfall at the model grid spacing scale, similar to the estimation using the CMDTE, the topographic effect is shown on large-scale rainfall distribution and heavy rainfall prediction. In a comparison using the CMDTE spectra, the experiments with and without topography have comparable unsaturated CMDTE at large scales (figure not shown). However, the experiments with topography resulted in higher scores of rainfall at larger scales, providing a different point of view on the topographic effect on predictability. Terrain-affected precipitation is a worldwide phenomenon. The examination of the predictability of rainfall here suggests that the model might better capture heavy rainfall near mountains than over plain areas. Meanwhile, the prediction of accumulated rainfall, rather than hourly rainfall, could be more predictable near mountains.

5. Discussion about the topographic effects on error growth

We investigated the impacts of topography and background winds on error growth and the predictability limit of thunderstorms. The impact of background winds is understandable because the background flow conditions determine the degree of the chaotic nature of a dynamical system. In comparison,

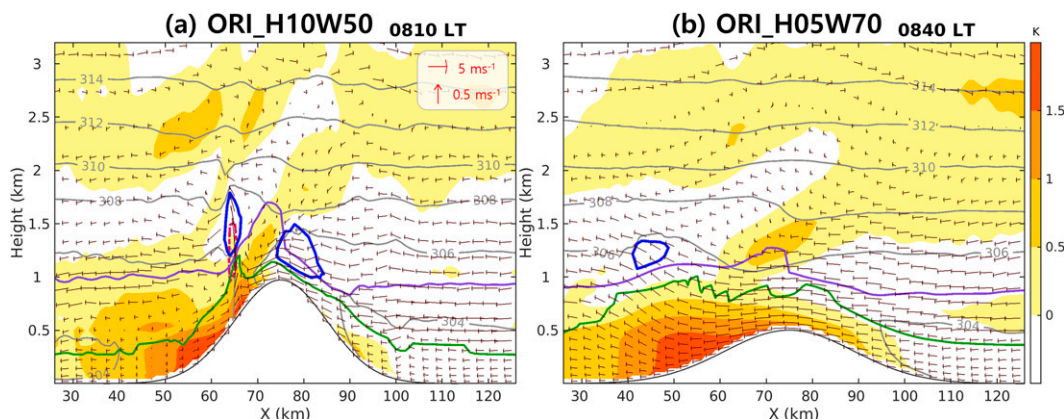


FIG. 11. Cross section in the x direction (see red dotted lines in Figs. 2c,e) of θ anomaly (color shaded), wind (arrows) in the control simulation of (a) ORI_H10W50 at 0810 LT and (b) ORI_H05W70 at 0840 LT. The blue solid and red dashed-dotted contours show the hydrometeors (0.1 g kg^{-1}) and updraft (0.5 m s^{-1}), respectively. The purple and green curves represent the height of the LFC and the thickness of the absolute unstable layer, respectively. The gray curves show the θ distribution. The red arrow and text in (a) show the scales for the purely horizontal and vertical wind vectors.

the impacts of topography are less straightforward. Previous results showed that mountain topography constrains the error growth associated with moist convection in the early stages of convection development, while this impact on error growth did not continue to later times, and thus, the range of predictability limit is affected little by topography. Thus, in this section, we investigate the experiment with topography in more detail to determine possible reasons for the topographic effect and its sensitivity to mountain geometry and background winds.

In the following, we will show a series of cross sections of θ anomaly and wind of the control simulation during CI in each experiment. The positive θ anomaly represents warmer air compared to the horizontally average θ at the same vertical level. In the cross-section figures, some wind vectors could point upward visibly, which might result from a very small horizontal wind but not a strong vertical wind. Therefore, we note that the contours of vertical winds are also depicted to reference the convective core.

First, we examined the sensitivity of the topographic effect to mountain heights. To show a more obvious difference between the experiments with different mountain heights, we compared ORI_H10W50 with ORI_H05W70 (Fig. 11). Similar conclusions can be drawn by comparing ORI_H10W50 and ORI_H05W50, as well as ORI_H10W70 and ORI_H05W70. In the cross sections of both ORI_H10W50 and ORI_H05W70, there is a positive θ anomaly on the lee side (i.e., west) of the mountain with respect to the prevailing low-level easterly wind resulting from the initial wind profile (Fig. 1). Simultaneously, the wind on the lee side is weak before sunrise because of the mountain block; this weak wind area is clearer in ORI_H10W50 than in ORI_H05W70 (figure not shown). After the sun rises at around 0450 LT in the early morning, the solar heating on the surface of the mountain slope leads to the difference in temperature

between the air near the mountain slope surface and the air away from the mountain at the same altitude, which generates positive buoyancy over the mountain slope and drives upslope wind. On the lee (i.e., west) side of the mountain in ORI_H10W50, a clearer temperature difference (Fig. 11a), accompanied by a condition of weaker wind than ORI_H10W70, drive the thermally driven upslope wind near the surface. This thermally driven upslope wind on the lee side blows to the east and encounters the prevailing low-level easterly wind over the mountain slope, generating convective clouds (e.g., at $x = 65 \text{ km}$ in Fig. 11a). Similar mechanisms of CI have also been indicated by previous studies (e.g., Banta and Schaaf 1987; Chen et al. 2002; Hagen et al. 2011; Hassanzadeh et al. 2016).

In ORI_H05W70 (Fig. 11b), however, the mountain is not high enough to trigger the thermally driven upslope wind on the lee side and is lower than the LFC. LFC is an altitude at which a saturated parcel diabatically lifted following the saturated adiabatic lapse rate becomes warmer than the environment. The warmer parcel can continue the upward motion without other external force. If the mountain is higher than the LFC, the air might have a chance to be lifted over the LFC and continue developing deep moist convection, while this is not the case in ORI_H05W70. Therefore, the prevailing easterly wind cannot trigger deep convection on the windward side either. Consequently, the deep convection was not initiated until the absolute unstable layer in which θ decreases with height due to solar heating becomes sufficiently thick. With such a deep, unstable layer, the low-level air parcels are lifted above the LFC and hence become convective clouds even with weaker upward wind triggered by the positive θ anomaly. This CI process over a heated mountain is considered to result in higher uncertainty of upward wind than in ORI_H10W50, leading to more rapid error growth. We note that the CI time in ORI_H05W70 was indeed earlier than

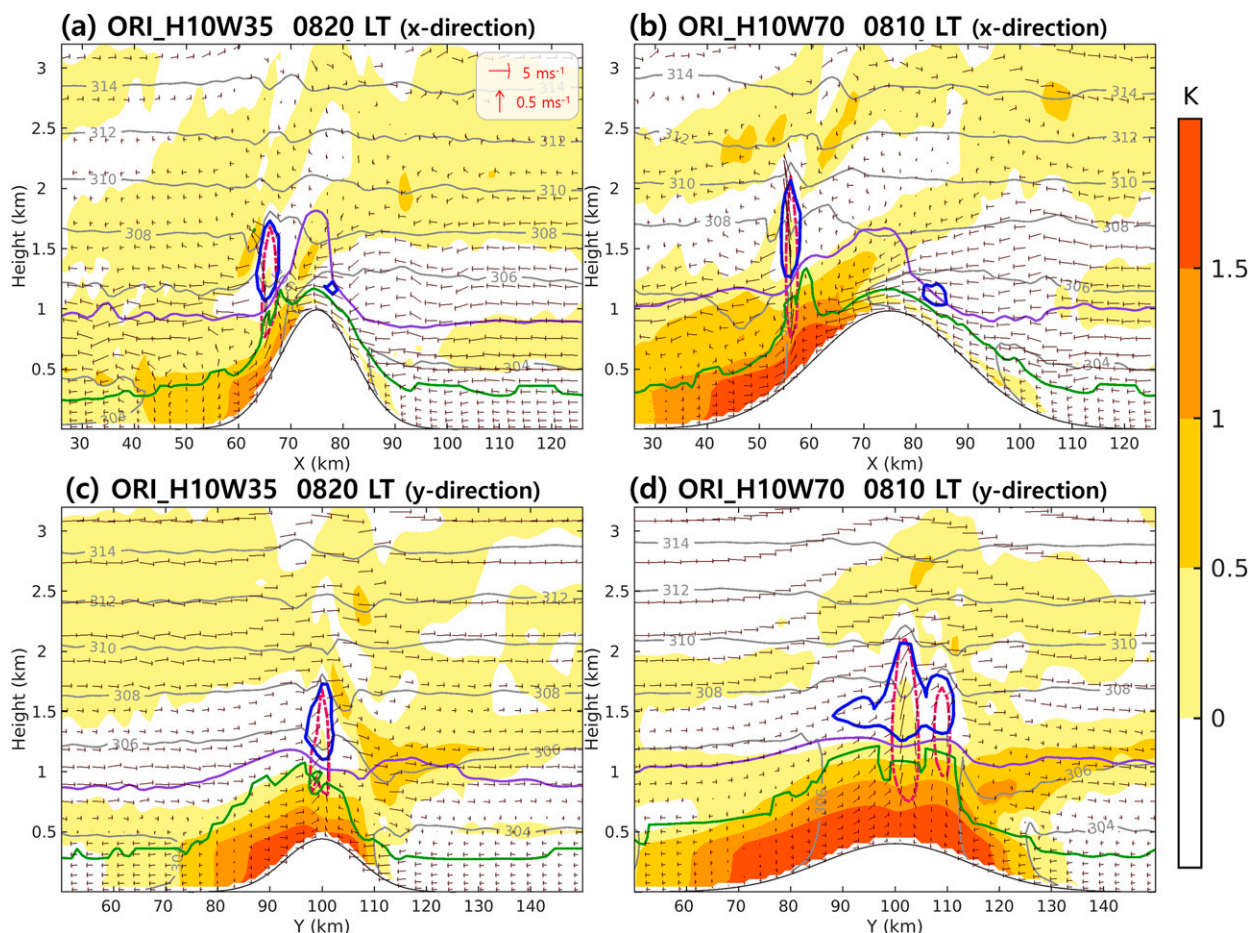


FIG. 12. As in Fig. 11, but for (a),(c) ORI_H10W35 and (b),(d) ORI_H10W70 and for (c),(d) the y direction. Refer to the red dotted lines in Figs. 2d and 2f for the location of the cross section.

that in ORI_H00W00, while the error growth in these two experiments was comparable (Figs. 4b and 5a,c). In other words, Fig. 11 suggests that it is the nature, rather than the time, of CI that causes slower error growth in the experiment with a 1000-m mountain.

We then compared the experiment with different mountain widths. To clearly illustrate the difference, ORI_H10W35 and ORI_H10W70 were examined. In both ORI_H10W35 and ORI_H10W70, deep moist convection was initiated on the lee side by the thermally driven westerly wind converging with the prevailing easterly wind along the x direction (Figs. 12a,b). The difference is shown in the cross section along the y direction (Figs. 12c,d). In ORI_H10W70, the area of positive θ anomaly is broader than that in ORI_H10W35, and the convergence area in the y direction also seems to be wider. Consequently, low-level air parcels have more chances to rise, which implies more uncertainty about the location of CI, resulting in more chances of triggering error growth in ORI_H10W70. In comparison, the narrower convergence area of ORI_H10W35 could result in lower uncertainty of updraft within a concentrated area, leading to a smaller error at the early stage of convection development (refer to Fig. 4a or Fig. 7c).

The findings of the different mechanisms for CI and its impact on error growth induced an investigation of the convective processes in the experiments with different background winds (Fig. 13). In U00_H10W50, the convection is triggered by the thermally driven upslope winds from both sides of the mountain and develops over the mountain top (Fig. 13b); the convective cloud almost stays at the same location and keeps developing vertically (Fig. 13d). With the convective cloud developing at the same place, the latent heat release from the condensation of water vapor keeps heating the air, resulting in a large positive θ anomaly. A positive θ anomaly means warmer air than the horizontally surrounding air, indicating positive buoyancy. Positive buoyancy could further enhance upward motion, inducing stronger convection, which triggers more error growth. Therefore, a small initial difference in the location of upward motion and cloud formation could rapidly grow during convection development. In this way, diabatic heating from moist convective processes provides positive feedback on error growth. This positive feedback triggered rapid error growth in U00_H10W50 when convection kept developing at the same place. Therefore, although the convection in U00_H10W50 is also initiated by the convergence of

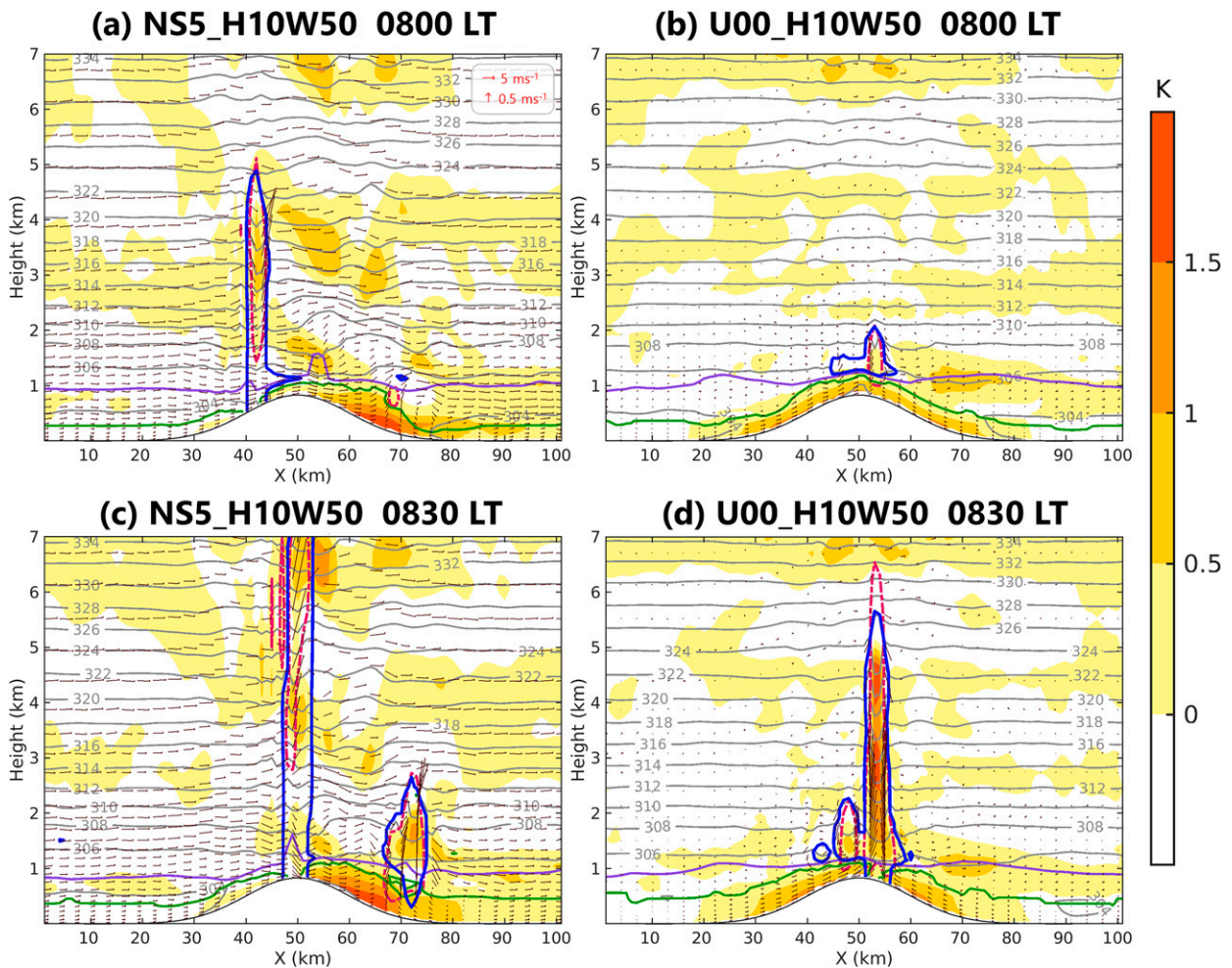


FIG. 13. As in Fig. 11, but for (a),(c) NS5_H10W50 and (b),(d) U00_H10W50 at (a),(b) 0800 and (c),(d) 0830 LT, respectively. Refer to the red dotted lines in Figs. 2h and 2j for the location of the cross section.

thermally induced circulations caused by the mountain, which could be a less uncertain process than the nonmountain case, the errors are still comparable in U00_H10W50 and U00_H00W00 (Fig. 4d).

In NS5_H10W50 (Figs. 13a,c), on the other hand, the lifting forced by the mountain on the windward (i.e., west) side induced the formation of clouds at an earlier time, around 0600 LT. The clouds keep developing and moving downstream without heating the air at the same place by latent heat release, resulting in a weaker positive θ anomaly and hence weaker upward wind than U00_H10W50. Meanwhile, similar to ORI_H10W50, the prevailing westerly flow in NS5_H10W50 encounters with the thermally induced upslope wind on the lee (i.e., east) side of the mountain (at around $x = 70$ km in Fig. 13a), triggering deep convection. With this similar CI mechanism and without the positive feedback of latent heating, NS5_H10W50 consequently results in topographic effects comparable to ORI_H10W50 (cf. Figs. 4a,c).

The time–height cross section of the error and convective clouds further links the relationship between diabatic heating

and the rapid error growth in NS5_H10W50 and U00_H10W50 (Fig. 14). In U00_H10W50, the amount of cloud increases rapidly, and the maximum upward wind reaches 15 m s^{-1} , indicating stronger moist convection only 1 h after the cloud formed. Simultaneously, the positive θ anomaly also reaches 4 K, and the error grows with an order of magnitude, from 10^{-3} to over $10^{-2} \text{ J kg}^{-1}$ (Fig. 14b). In NS5_H10W50, on the other hand, the cloud amount, upward wind, and positive θ anomaly did not reach the same level as in U00_H10W50 until 0900 LT, and the error grew slowly before that time (Fig. 14a). A similar trend of the error and cloud amounts was also seen in the ORI experiments (Fig. 5). The present analysis of NS5_H10W50 and U00_H10W50 suggests that latent heat release is critical for triggering the rapid error growth associated with moist convection. When convection continues developing, the positive feedback from diabatic heating could make the impact of topography on error growth almost negligible. The rapid error growth dominated by convection development eventually limits predictability at the maximum convective activity time, as shown in the previous section, regardless of the presence of topography.

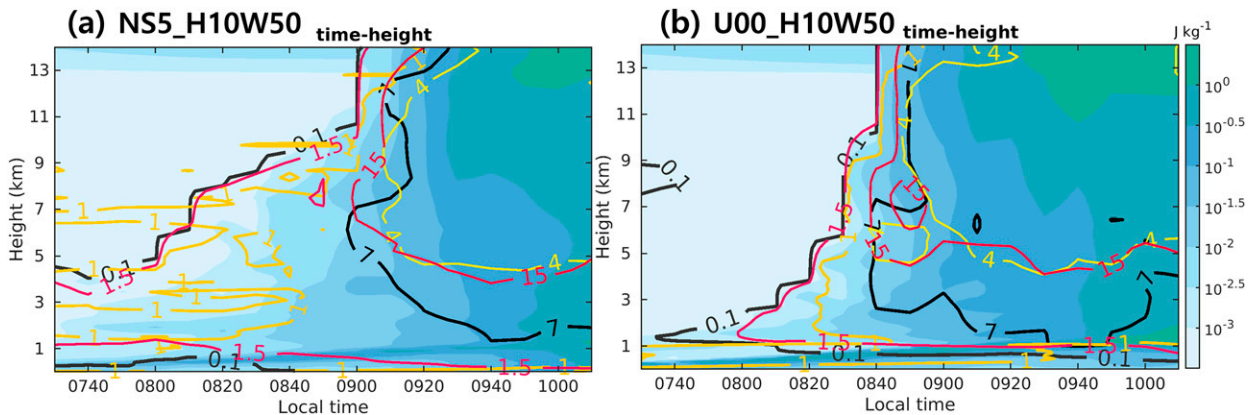


FIG. 14. As in Fig. 5, but for (a) NS5_H10W50 and (b) U00_H10W50.

6. Summary

This study assessed the impact of topography and background flows on error growth and the predictability associated with thermally induced thunderstorms. We conducted simulations of thunderstorms under different topography conditions and background flows using the Weather Research and Forecasting (WRF) Model in an idealized framework. Using these simulations, identical twin experiments were performed to investigate error growth and predictability. The predictability of thunderstorms was evaluated using the differences between the simulations in model state variables and rainfall. The difference in model states is estimated by a proposed metric, convective moist different total energy (CMDTE), and that of rainfall is assessed by the fractions skill score (FSS).

The topographic effect on error growth triggered by moist convection was assessed. The convection initiated under the impact of mountains triggered less error growth than the case with flat topography, showing a topographic effect on constraining error growth. This topographic effect is sensitive to mountain heights and widths. The mountain of 1000-m height shows the impact on error growth, while the experiments with 500-m height tend to have comparable errors to those without topography. For mountains of the same height, the topographic effects of a narrower mountain tend to be clearer.

The topographic effect and its sensitivity to mountain geometry are caused by different natures in the convection initiation (CI) induced by mountains with different widths and heights. For a higher mountain that can trigger thermally induced upslope wind on the lee side with respect to the presence of background flow, the error grows less rapidly at first when the moist convection is initiated by the thermally induced upslope wind converging with the background flow. For a lower mountain that cannot trigger the thermally driven upslope wind on the lee side, moist convection does not develop until the absolute unstable layer built by solar heating becomes thick enough to push the air over the level of free convection. The underlying convective instability is then considered to contribute to rapid error growth, similar to the case without a mountain. Mountain width also plays a role. A narrower mountain would build a narrower area for convection

to develop, resulting in less uncertainty about the location of forming convective clouds. Consequently, errors grow less rapidly compared to the case of a wider mountain when convection is initiated. Our findings regarding the different CI mechanisms and their impact on error growth highlight the different chaotic natures of the moist convection that develops in the presence of mountain topography, which is seldom discussed in previous studies. Further studies should investigate the uncertainty of different CI mechanisms in mountain areas.

The results also indicate the sensitivity of the topographic effect on error growth to background winds. For experiments with different background winds, a similar restraining effect of topography on error growth is less clear in experiments with zero background wind. Further analysis revealed that the diabatic heating caused by latent heat release in convective clouds might be a key component that triggers rapid error growth in the no-wind case. For the experiments with mountain topography and zero background wind, the convective clouds stayed at the same place and keep heating the air. The diabatic heating in clouds results in a positive anomaly of temperature that provides further buoyancy forcing and facilitates the development of convective clouds and the subsequent error growth. The differences in convection development led to more different diabatic heating and, thus, more differences in the continuous development of convection, resulting in positive feedback on error growth. This positive feedback makes the topographic effects on error growth unclear in experiments without a background wind.

The positive feedback of diabatic heating is also considered to be the process that dominates error growth so greatly that the mountain topography used in this study has little impact at later times. The results showed that, regardless of the existence of the mountain, the errors became comparable among the experiments after the convection continued developing. It is considered that after convection becomes more active, topography stops affecting the nature of moist convection and the rapid error growth. The rapid error growth accompanying the convection development then leads to the error saturation, implying the loss of predictability after the activity of

thermally induced thunderstorms reaches the maximum. Consequently, the mountain topography used here affects little of this predictability limit. Similarly, smaller initial errors or starting the simulation later did not break the limit of predictability determined by the time of the maximum convective activity. In comparison, the background flows, which change the evolution of convection itself, influence the predictability limit of thermally induced thunderstorms more than the topography tested in this study. This impact of background flows is consistent with existing knowledge about flow-dependent predictability. The perturbed simulations that were started later but showed the same timing of losing predictability further serve to emphasize the strong flow-dependent properties at convective scales. It is also worth noting that our investigation of the impact of topography showed a unique feature of strongly flow-dependent predictability at convective scales differing from that at synoptic scales: slow error growth at first does not necessarily result in longer predictable time.

We also examined the predictability of the rainfall caused by thunderstorms using the FSS. The predictability limit suggested by the scores of hourly rainfall on the model grid spacing scale is similar to that estimated by the CMDTE. Background winds show a greater impact on hourly rainfall performance than topography. In comparison, the hourly rainfall FSS at larger scales tended to become less noticeable between the experiments with different background winds, while the impact of topography was more apparent at larger-scale rainfall distribution. The useful scale suggested by the skillful criteria of the FSS is generally finer in the experiment with topography than without. The impact of mountains on the large-scale rainfall distribution is considered as one of the reasons for the topographic effect in terms of several-hour accumulated rainfall. Even at the model grid spacing scale, experiments with topography can have higher scores throughout the 12-h accumulation period than the nonmountain case. Additionally, the experiments with topography showed higher scores when larger rainfall thresholds were used, implying the impact of topography on heavier rainfall. The effects of topography on accumulated and strong rainfalls are also sensitive to the different background winds, highlighting the intertwined effects of topography and background winds.

In this study, the rapid error growth dynamics associated with moist convection and the highly limited predictability are generally consistent with previous studies (Zhang et al. 2003; Zhang et al. 2016; Weyn and Durran 2017, 2019; Bachmann et al. 2019). We note that in the current study, the idealized model configurations were used, and only one atmospheric stability condition provided by the sounding data was considered, which might limit the universality of our results. Nevertheless, although only one atmospheric stability condition is considered here, our simulations of moist convection near mountain topography resemble those presented in previous studies (e.g., Hassanzadeh et al. 2016; Bachmann et al. 2019; Mulholland et al. 2020). Thus, we believe that our results showed one common scenario of how moist convection develops around mountains and can be used to assess the impact of topography on error growth and predictability associated with moist convection. Further studies could be done with other

combinations of background flows and topography or even with more realistic model configurations.

Regardless of the limit of an idealized configuration, this study systematically demonstrates the impact of topography and background flow on the predictability limit of thunderstorms and accompanying rainfall, providing new insights into convective-scale predictability. Summarily, the rapid error growth and the subsequent loss of predictability of thunderstorms are highly related to the properties of moist convection, from the initiation mechanism to the processes during development. The factors that can change the mechanisms during convection initiation and development can also result in different error growth and predictability. Regarding background flow conditions, the impact on the duration of convection life cycles results in different levels of predictability. In terms of topography, when the topography plays a role in inducing the CI less uncertainly, errors grow less rapidly at first. However, this topographic effect may not be maintained when the latent heat released by the moist processes in clouds triggers more intense convective activities. Dominated by the underlying dynamics of moist convection, error growth is strongly flow dependent that slower error growth at first does not change the timing of losing predictability. Consequently, mountain topography affects little on the predictability limit estimated by the error saturation of the model state variables.

When trying to improve the prediction of thunderstorms, the chaotic nature of thunderstorms might limit the space for improving instantaneous deterministic dynamical predictions even with better initial conditions or model configuration. Rather than improving deterministic dynamical predictions, we can focus on developing ensemble prediction systems that better represent the uncertainty of convection development. For example, our results showing the topographic effect suggested the possibility of less uncertain CI over mountains as long as the mechanism is accurately captured in numerical models. Nevertheless, in more realistic cases, the representation of atmospheric conditions is usually less accurate over complex terrains because of the model deficiency. Environmental conditions are also usually not perfectly captured, providing an additional source of errors. From this aspect of real-life NWP models, our results imply that the uncertainty of predicting CI over mountains might be underestimated by an ensemble prediction system whose perturbation is only added to the initial condition. Because the ensemble spread could grow slower during CI over mountains, while the model barely represents the real atmosphere, leading to the overly optimistic estimation of the forecast error estimated by the ensemble spread. In this case, other perturbations, such as those on model parameterization or boundary conditions, must be considered to build a more effective ensemble prediction system.

Other efforts could statistically analyze the environmental conditions favored by deep moist convection to guide the occurrence of thunderstorms (e.g., Lin et al. 2012; Chen et al. 2016; Chang et al. 2017) or even to indicate the flow-dependent predictability of a specific day. Meanwhile, the estimation using rainfall provides another aspect of the impact of topography. The results of topographic effects on rainfall encourage more

confident use of accumulated rainfall, rather than hourly rainfall, over mountain areas. Additionally, predictions of heavy rainfall produced by thunderstorms near mountains could be trusted more than those over plain areas.

Acknowledgments. This study was partly supported by the Japan Society for the Promotion of Science (JSPS) Scientific Research Grants 20H00289 and 21H01591 and by the Japan Ministry of Education, Culture, Sports, Science and Technology (MEXT) under the “Program for Promoting Researches on the Supercomputer Fugaku” (Large Ensemble Atmospheric and Environmental Prediction for Disaster Prevention and Mitigation, JPMXP1020200305, ID: hp210166, hp220167). Some of the content in this work was based on the doctoral dissertation of Pin-Ying Wu, which can be found at <https://doi.org/10.14989/doctor.k24124>. The authors thank Dr. Takuya Kawabata from the Meteorological Research Institute for his valuable discussions.

Data availability statement. The sounding data used for initializing the simulation are available from the Japan Meteorological Agency (JMA) at <https://www.data.jma.go.jp/obd/stats/etrn/upper/index.php?year=2019&month=8&day=19&hour=9&atm=&point=47778>.

REFERENCES

- Bachmann, K., C. Keil, and M. Weissmann, 2019: Impact of radar data assimilation and orography on predictability of deep convection. *Quart. J. Roy. Meteor. Soc.*, **145**, 117–130, <https://doi.org/10.1002/qj.3412>.
- , —, G. C. Craig, M. Weissmann, and C. A. Welzbacher, 2020: Predictability of deep convection in idealized and operational forecasts: Effects of radar data assimilation, orography, and synoptic weather regime. *Mon. Wea. Rev.*, **148**, 63–81, <https://doi.org/10.1175/MWR-D-19-0045.1>.
- Banta, R. M., and C. B. Schaaf, 1987: Thunderstorm genesis zones in the Colorado Rocky Mountains as determined by traceback of geosynchronous satellite images. *Mon. Wea. Rev.*, **115**, 463–476, [https://doi.org/10.1175/1520-0493\(1987\)115<0463: TGZITC>2.0.CO;2](https://doi.org/10.1175/1520-0493(1987)115<0463: TGZITC>2.0.CO;2).
- Bauer, P., A. Thorpe, and G. Brunet, 2015: The quiet revolution of numerical weather prediction. *Nature*, **525**, 47–55, <https://doi.org/10.1038/nature14956>.
- Carbone, R. E., W. A. Cooper, and W.-C. Lee, 1995: Forcing of flow reversal along the windward slopes of Hawaii. *Mon. Wea. Rev.*, **123**, 3466–3480, [https://doi.org/10.1175/1520-0493\(1995\)123<3466:FOFRAT>2.0.CO;2](https://doi.org/10.1175/1520-0493(1995)123<3466:FOFRAT>2.0.CO;2).
- , J. D. Tuttle, D. A. Ahijevych, and S. B. Trier, 2002: Inferences of predictability associated with warm season precipitation episodes. *J. Atmos. Sci.*, **59**, 2033–2056, [https://doi.org/10.1175/1520-0469\(2002\)059<2033:IOPAWW>2.0.CO;2](https://doi.org/10.1175/1520-0469(2002)059<2033:IOPAWW>2.0.CO;2).
- Chang, H.-L., B. G. Brown, P.-S. Chu, Y.-C. Liou, and W.-H. Wang, 2017: Nowcast guidance of afternoon convection initiation for Taiwan. *Wea. Forecasting*, **32**, 1801–1817, <https://doi.org/10.1175/WAF-D-16-0224.1>.
- Changnon, S. A., 2001: Damaging thunderstorm activity in the United States. *Bull. Amer. Meteor. Soc.*, **82**, 597–608, [https://doi.org/10.1175/1520-0477\(2001\)082<0597:DTAITU>2.3.CO;2](https://doi.org/10.1175/1520-0477(2001)082<0597:DTAITU>2.3.CO;2).
- Chen, C.-S., and C.-Y. Lin, 1997: A numerical study of airflow over Taiwan Island. *Atmos. Environ.*, **31**, 463–473, [https://doi.org/10.1016/S1352-2310\(96\)00191-4](https://doi.org/10.1016/S1352-2310(96)00191-4).
- , —, Y.-J. Chuang, and H.-C. Yeh, 2002: A study of afternoon heavy rainfall in Taiwan during the mei-yu season. *Atmos. Res.*, **65**, 129–149, [https://doi.org/10.1016/S0169-8095\(02\)00061-3](https://doi.org/10.1016/S0169-8095(02)00061-3).
- Chen, T.-C., J.-D. Tsay, and E. S. Takle, 2016: A forecast advisory for afternoon thunderstorm occurrence in the Taipei basin during summer developed from diagnostic analysis. *Wea. Forecasting*, **31**, 531–552, <https://doi.org/10.1175/WAF-D-15-0082.1>.
- Cheng, H.-W., S.-C. Yang, Y.-C. Liou, and C.-S. Chen, 2020: An investigation of the sensitivity of predicting a severe rainfall event in northern Taiwan to the upstream condition with a WRF-based radar data assimilation system. *SOLA*, **16**, 97–103, <https://doi.org/10.2151/sola.2020-017>.
- Demko, J. C., B. Geerts, Q. Miao, and J. A. Zehnder, 2009: Boundary layer energy transport and cumulus development over a heated mountain: An observational study. *Mon. Wea. Rev.*, **137**, 447–468, <https://doi.org/10.1175/2008MWR2467.1>.
- Done, J. M., G. C. Craig, S. L. Gray, and P. A. Clark, 2012: Case-to-case variability of predictability of deep convection in a mesoscale model. *Quart. J. Roy. Meteor. Soc.*, **138**, 638–648, <https://doi.org/10.1002/qj.943>.
- Durrander, D. R., and M. Gingrich, 2014: Atmospheric predictability: Why butterflies are not of practical importance. *J. Atmos. Sci.*, **71**, 2476–2488, <https://doi.org/10.1175/JAS-D-14-0007.1>.
- , and J. A. Weyn, 2016: Thunderstorms do not get butterflies. *Bull. Amer. Meteor. Soc.*, **97**, 237–243, <https://doi.org/10.1175/BAMS-D-15-00070.1>.
- Ehrendorfer, M., R. M. Errico, and K. D. Raeder, 1999: Singular-vector perturbation growth in a primitive equation model with moist physics. *J. Atmos. Sci.*, **56**, 1627–1648, [https://doi.org/10.1175/1520-0469\(1999\)056<1627:SVPGIA>2.0.CO;2](https://doi.org/10.1175/1520-0469(1999)056<1627:SVPGIA>2.0.CO;2).
- Flesch, T. K., and G. W. Reuter, 2012: WRF Model simulation of two Alberta flooding events and the impact of topography. *J. Hydrometeorol.*, **13**, 695–708, <https://doi.org/10.1175/JHM-D-11-035.1>.
- Froude, L. S. R., L. Bengtsson, and K. I. Hodges, 2013: Atmospheric predictability revisited. *Tellus*, **65A**, 19022, <https://doi.org/10.3402/tellusa.v65i0.19022>.
- Fu, D., and X. Guo, 2012: A cloud-resolving simulation study on the merging processes and effects of topography and environmental winds. *J. Atmos. Sci.*, **69**, 1232–1249, <https://doi.org/10.1175/JAS-D-11-049.1>.
- Hagen, M., J. van Baelen, and E. Richard, 2011: Influence of the wind profile on the initiation of convection in mountainous terrain. *Quart. J. Roy. Meteor. Soc.*, **137**, 224–235, <https://doi.org/10.1002/qj.784>.
- Hassanzadeh, H., J. Schmidli, W. Langhans, L. Schlemmer, and C. Schär, 2016: Impact of topography on the diurnal cycle of summertime moist convection in idealized simulations. *Meteor. Z.*, **25**, 181–194, <https://doi.org/10.1127/metz/2015/0653>.
- Hohenegger, C., and C. Schär, 2007a: Atmospheric predictability at synoptic versus cloud-resolving scales. *Bull. Amer. Meteor. Soc.*, **88**, 1783–1794, <https://doi.org/10.1175/BAMS-88-11-1783>.
- , and —, 2007b: Predictability and error growth dynamics in cloud-resolving models. *J. Atmos. Sci.*, **64**, 4467–4478, <https://doi.org/10.1175/2007JAS2143.1>.
- , D. Lüthi, and C. Schär, 2006: Predictability mysteries in cloud-resolving models. *Mon. Wea. Rev.*, **134**, 2095–2107, <https://doi.org/10.1175/MWR3176.1>.
- Imamovic, A., L. Schlemmer, and C. Schär, 2019: Mountain volume control on deep-convective rain amount during episodes

- of weak synoptic forcing. *J. Atmos. Sci.*, **76**, 605–626, <https://doi.org/10.1175/JAS-D-18-0217.1>.
- Johnson, A., and Coauthors, 2014: Multiscale characteristics and evolution of perturbations for warm season convection-allowing precipitation forecasts: Dependence on background flow and method of perturbation. *Mon. Wea. Rev.*, **142**, 1053–1073, <https://doi.org/10.1175/MWR-D-13-00204.1>.
- Judt, F., 2018: Insights into atmospheric predictability through global convection-permitting model simulations. *J. Atmos. Sci.*, **75**, 1477–1497, <https://doi.org/10.1175/JAS-D-17-0343.1>.
- , 2020: Atmospheric predictability of the tropics, middle latitudes, and polar regions explored through global storm-resolving simulations. *J. Atmos. Sci.*, **77**, 257–276, <https://doi.org/10.1175/JAS-D-19-0116.1>.
- Kerns, B. W. J., Y.-L. Chen, and M.-Y. Chang, 2010: The diurnal cycle of winds, rain, and clouds over Taiwan during the mei-yu, summer, and autumn rainfall regimes. *Mon. Wea. Rev.*, **138**, 497–516, <https://doi.org/10.1175/2009MWR3031.1>.
- Leoncini, G., R. S. Plant, S. L. Gray, and P. A. Clark, 2010: Perturbation growth at the convective scale for CSIP IOP18. *Quart. J. Roy. Meteor. Soc.*, **136**, 653–670, <https://doi.org/10.1002/qj.587>.
- Lin, P.-F., P.-L. Chang, B. J.-D. Jou, J. W. Wilson, and R. D. Roberts, 2012: Objective prediction of warm season afternoon thunderstorms in northern Taiwan using a fuzzy logic approach. *Wea. Forecasting*, **27**, 1178–1197, <https://doi.org/10.1175/WAF-D-11-00105.1>.
- Lorenz, E. N., 1969: The predictability of a flow which possesses many scales of motion. *Tellus*, **21**, 289–307, <https://doi.org/10.3402/tellusa.v21i3.10086>.
- Melhauser, C., and F. Zhang, 2012: Practical and intrinsic predictability of severe and convective weather at the mesoscales. *J. Atmos. Sci.*, **69**, 3350–3371, <https://doi.org/10.1175/JAS-D-11-0315.1>.
- Miglietta, M. M., A. Manzato, and R. Rotunno, 2016: Characteristics and predictability of a supercell during HyMeX SOP1. *Quart. J. Roy. Meteor. Soc.*, **142**, 2839–2853, <https://doi.org/10.1002/qj.2872>.
- Mulholland, J. P., S. W. Nesbitt, R. J. Trapp, and J. M. Peters, 2020: The influence of terrain on the convective environment and associated convective morphology from an idealized modeling perspective. *J. Atmos. Sci.*, **77**, 3929–3949, <https://doi.org/10.1175/JAS-D-19-0190.1>.
- Muller, C., 2013: Impact of convective organization on the response of tropical precipitation extremes to warming. *J. Climatol.*, **26**, 5028–5043, <https://doi.org/10.1175/JCLI-D-12-00655.1>.
- Ngan, K., and G. E. Eperon, 2012: Middle atmosphere predictability in a numerical weather prediction model: Revisiting the inverse error cascade. *Quart. J. Roy. Meteor. Soc.*, **138**, 1366–1378, <https://doi.org/10.1002/qj.984>.
- Nielsen, E. R., and R. S. Schumacher, 2016: Using convection-allowing ensembles to understand the predictability of an extreme rainfall event. *Mon. Wea. Rev.*, **144**, 3651–3676, <https://doi.org/10.1175/MWR-D-16-0083.1>.
- Nomura, S., and T. Takemi, 2011: Environmental stability for afternoon rain events in the Kanto Plain in summer. *SOLA*, **7**, 9–12, <https://doi.org/10.2151/sola.2011-003>.
- Palmer, T. N., A. Döring, and G. Seregin, 2014: The real butterfly effect. *Nonlinearity*, **27**, R123, <https://doi.org/10.1088/0951-7715/27/9/R123>.
- Potvin, C. K., E. M. Murillo, M. L. Flora, and D. M. Wheatley, 2017: Sensitivity of supercell simulations to initial-condition resolution. *J. Atmos. Sci.*, **74**, 5–26, <https://doi.org/10.1175/JAS-D-16-0098.1>.
- Roberts, N. M., and H. W. Lean, 2008: Scale-selective verification of rainfall accumulations from high-resolution forecasts of convective events. *Mon. Wea. Rev.*, **136**, 78–97, <https://doi.org/10.1175/2007MWR2123.1>.
- Rotunno, R., and C. Snyder, 2008: A generalization of Lorenz's model for the predictability of flows with many scales of motion. *J. Atmos. Sci.*, **65**, 1063–1076, <https://doi.org/10.1175/2007JAS2449.1>.
- Schmidli, J., S. Böing, and O. Fuhrer, 2018: Accuracy of simulated diurnal valley winds in the Swiss Alps: Influence of grid resolution, topography filtering, and land surface datasets. *Atmosphere*, **9**, 196, <https://doi.org/10.3390/atmos9050196>.
- Selz, T., and G. C. Craig, 2015: Upscale error growth in a high-resolution simulation of a summertime weather event over Europe. *Mon. Wea. Rev.*, **143**, 813–827, <https://doi.org/10.1175/MWR-D-14-00140.1>.
- Sun, Y. Q., and F. Zhang, 2016: Intrinsic versus practical limits of atmospheric predictability and the significance of the butterfly effect. *J. Atmos. Sci.*, **73**, 1419–1438, <https://doi.org/10.1175/JAS-D-15-0142.1>.
- , and —, 2020: A new theoretical framework for understanding multiscale atmospheric predictability. *J. Atmos. Sci.*, **77**, 2297–2309, <https://doi.org/10.1175/JAS-D-19-0271.1>.
- , R. Rotunno, and F. Zhang, 2017: Contributions of moist convection and internal gravity waves to building the atmospheric $-5/3$ kinetic energy spectra. *J. Atmos. Sci.*, **74**, 185–201, <https://doi.org/10.1175/JAS-D-16-0097.1>.
- Takemi, T., 2014: Characteristics of summertime afternoon rainfall and its environmental conditions in and around the Nobi Plain. *SOLA*, **10**, 158–162, <https://doi.org/10.2151/sola.2014-033>.
- , and R. Rotunno, 2003: The effects of subgrid model mixing and numerical filtering in simulations of mesoscale cloud systems. *Mon. Wea. Rev.*, **131**, 2085–2101, [https://doi.org/10.1175/1520-0493\(2003\)131<2085:TEOSMM>2.0.CO;2](https://doi.org/10.1175/1520-0493(2003)131<2085:TEOSMM>2.0.CO;2).
- , and S. Tsuchida, 2014: Statistical analysis on precipitation events over the Kinki District, Japan in summer (in Japanese with an English abstract). *Annu. Disaster Prev. Res. Inst., Kyoto Univ.*, **57B**, 216–238.
- Vergeiner, I., and E. Dreiseitl, 1987: Valley winds and slope winds—Observations and elementary thoughts. *Meteor. Atmos. Phys.*, **36**, 264–286, <https://doi.org/10.1007/BF01045154>.
- Wallace, J. M., 1975: Diurnal variations in precipitation and thunderstorm frequency over the conterminous United States. *Mon. Wea. Rev.*, **103**, 406–419, [https://doi.org/10.1175/1520-0493\(1975\)103<0406:DVIPAT>2.0.CO;2](https://doi.org/10.1175/1520-0493(1975)103<0406:DVIPAT>2.0.CO;2).
- Walser, A., D. Lüthi, and C. Schär, 2004: Predictability of precipitation in a cloud-resolving model. *Mon. Wea. Rev.*, **132**, 560–577, [https://doi.org/10.1175/1520-0493\(2004\)132<0560:POPIAC>2.0.CO;2](https://doi.org/10.1175/1520-0493(2004)132<0560:POPIAC>2.0.CO;2).
- Weyn, J. A., and D. R. Durran, 2017: The dependence of the predictability of mesoscale convective systems on the horizontal scale and amplitude of initial errors in idealized simulations. *J. Atmos. Sci.*, **74**, 2191–2210, <https://doi.org/10.1175/JAS-D-17-0006.1>.
- , and —, 2018: Ensemble spread grows more rapidly in higher-resolution simulations of deep convection. *J. Atmos. Sci.*, **75**, 3331–3345, <https://doi.org/10.1175/JAS-D-17-0332.1>.
- , and —, 2019: The scale dependence of initial-condition sensitivities in simulations of convective systems over the southeastern United States. *Quart. J. Roy. Meteor. Soc.*, **145**, 57–74, <https://doi.org/10.1002/qj.3367>.

- Whiteman, C. D., 1990: Observations of thermally developed wind systems in mountainous terrain. *Atmospheric Processes over Complex Terrain*, Meteor. Monogr., No. 23, Amer. Meteor. Soc., 5–42, https://doi.org/10.1007/978-1-935704-25-6_2.
- Wu, N., X. Zhuang, J. Min, and Z. Meng, 2020: Practical and intrinsic predictability of a warm-sector torrential rainfall event in the South China monsoon region. *J. Geophys. Res. Atmos.*, **125**, e2019JD031313, <https://doi.org/10.1029/2019JD031313>.
- Wu, P.-Y., and T. Takemi, 2021: The impact of topography on the initial error growth associated with moist convection. *SOLA*, **17**, 134–139, <https://doi.org/10.2151/sola.2021-024>.
- , S.-C. Yang, C.-C. Tsai, and H.-W. Cheng, 2020: Convective-scale sampling error and its impact on the ensemble radar data assimilation system: A case study of a heavy rainfall event on 16 June 2008 in Taiwan. *Mon. Wea. Rev.*, **148**, 3631–3652, <https://doi.org/10.1175/MWR-D-19-0319.1>.
- Zhang, F., and D. Tao, 2013: Effects of vertical wind shear on the predictability of tropical cyclones. *J. Atmos. Sci.*, **70**, 975–983, <https://doi.org/10.1175/JAS-D-12-0133.1>.
- , C. Snyder, and R. Rotunno, 2003: Effects of moist convection on mesoscale predictability. *J. Atmos. Sci.*, **60**, 1173–1185, [https://doi.org/10.1175/1520-0469\(2003\)060<1173:EOMCOM>2.0.CO;2](https://doi.org/10.1175/1520-0469(2003)060<1173:EOMCOM>2.0.CO;2).
- , N. Bei, R. Rotunno, C. Snyder, and C. C. Epifanio, 2007: Mesoscale predictability of moist baroclinic waves: Convection-permitting experiments and multistage error growth dynamics. *J. Atmos. Sci.*, **64**, 3579–3594, <https://doi.org/10.1175/JAS4028.1>.
- , Y. Q. Sun, L. Magnusson, R. Buizza, S.-J. Lin, J.-H. Chen, and K. Emanuel, 2019: What is the predictability limit of midlatitude weather? *J. Atmos. Sci.*, **76**, 1077–1091, <https://doi.org/10.1175/JAS-D-18-0269.1>.
- Zhang, Y., F. Zhang, D. J. Stensrud, and Z. Meng, 2016: Intrinsic predictability of the 20 May 2013 tornadic thunderstorm event in Oklahoma at storm scales. *Mon. Wea. Rev.*, **144**, 1273–1298, <https://doi.org/10.1175/MWR-D-15-0105.1>.
- Zhuang, X., J. Min, L. Zhang, S. Wang, N. Wu, and H. Zhu, 2020: Insights into convective-scale predictability in East China: Error growth dynamics and associated impact on precipitation of warm-season convective events. *Adv. Atmos. Sci.*, **37**, 893–911, <https://doi.org/10.1007/s00376-020-9269-5>.